Three-dimensional laminar-turbulent transition simulations with the $\gamma - \overline{Re_{\theta t}}$ transition model

Jeremy Schembri

Master of Engineering

Department of Mechanical Engineering

McGill University

Montreal, Quebec

2015-12-09

A thesis submitted to McGill University in partial fulfilment of the requirements for the degree of Master of Engineering.

ABSTRACT

The location and length of the laminar-turbulent transition region is critical to the assessment of the aerodynamic performance of aircraft wings. Despite its importance, transition models are rarely included in engineering simulations because of challenges developing a complete model that accounts for the complex and multi-scale nature of various transitional processes. Additional challenges also exist in formulating a transition model that i) is compatible with current computational fluid dynamics approaches, ii) is able to simulate complex non-trivial geometries and iii) has an algorithm that scales efficiently on large parallel supercomputers. The aim of this research was to use a novel method called the $\gamma - \overline{Re_{\theta t}}$ transition model to demonstrate the ability to model complex transition for aerospace geometries. The $\gamma - \overline{Re_{\theta t}}$ transition model is a two transport-equation model that employs only local variables to calculate the intermittency and the transition onset criteria in terms of the local transition onset momentum thickness Reynolds number. The solution modifies the production of turbulent kinetic energy in the k-ω SST turbulence model to predict laminar, transitional and turbulent regions in the Reynolds-averaged Navier-Stokes equations. The proposed method was validated against experimental data for the NACA0012 and NLF(1)-0416 airfoils and the DLR-F5 aircraft wing.

ABRÉGÉ

La connaissance de l'emplacement ainsi que de la longueur de la zone de transition laminaire-turbulent est cruciale pour résoudre précisement des écoulements de paroi. Malgré l'importance de ce phénomène, les modèles de transition sont rarement utilisés en industrie. La complexité des processus de déclenchement, ainsi que les difficultés à formuler une approche compatible avec les méthodes numériques pour les écoulements à géométries complexes de l'aéronautique s'adaptant efficacement pour le calcul parallèle sur superordinateurs, sont les principaux facteurs qui limitent l'utilisation de ces modèles. L'objectif de ce travail de recherche était d'utiliser une nouvelle méthode intitulée modèle de transition $\gamma - \overline{Re_{\theta t}}$ afin de démontrer la modélisation de la transition sur des géométries complexes. Le modèle de transition $\gamma - \overline{Re_{\theta t}}$ est un modèle à deux équations de transport qui utilise uniquement des variables locales pour résoudre le critère de déclenchement de l'intermittence et de la transition. La solution de ce modèle est ensuite utilisée pour modifier la production d'énergie cinétique turbulente dans le modèle de turbulence k-ω SST afin de prédire l'emplacement des régions laminaires, transitoires et turbulentes dans la solution des équations de Navier-Stokes moyennées (RANS). La méthode proposée a été validée avec les données expérimentales pour les écoulements sur des profils d'ailes NACA0012 et NLF(1)-0416, ainsi que sur une aile d'avion DLR-F5.

ACKNOWLEDGEMENTS

I would like to thank my supervisor Siva Nadarajah for his enduring knowledge and wisdom over the course of my research. His patience combined with his passion was much appreciated and I am grateful for having his guidance throughout my studies. In addition, thanks to all of my colleagues and friends in McGill's Computational Aerodynamics and Design group. Whether it through insightful comments or friendly banter, you created an intellectually invigorating environment that was welcome to any conversation or idea. A special thanks to François Bisson for his help understanding three-dimensional flow, all the discussions about MPI with Pierre-Olivier Tardif and Doug Shi-Dong's insight on grid generation. I would like to extend gratitude to the Natural Sciences and Engineering Research Council of Canada (NSERC) and McGill's computational resources for their financial and material support. Above all, I would like to thank my father John Schembri, mother Kim Schembri and my siblings for their constant encouragement.

TABLE OF CONTENTS

LIST OF TABLES

LIST OF FIGURES

CHAPTER 1
Introduction

1.1 Motivation

As the aerospace industry pushes towards more efficient and optimized aircraft, accurately predicting a vehicle's aerodynamic characteristics is critical to its evaluation and design. The faster and more accurately the performance of an aircraft can be determined, the faster improvements can be studied and implemented. Evaluating the performance of an aircraft hinges on the ability to accurately simulate the fluid flow for a wide range of flow conditions. The principle methods used to study the fluid flow around an aircraft are analytical, experimental and computational. Deriving the full analytic solution is beyond current mathematical knowledge while experimental methods for commercial aircraft development are expensive and time consuming. The third method, computational fluid dynamics (CFD), is becoming a critical tool within industry and research as a result of increased access to high performance computing. The performance of computing is steadily improving though the complicated nature of industrial flows and the constraints of current computational resources limits engineers to various methods and models. The important physical phenomenon of laminar-turbulent transition does not yet have fully comprehensive and documented models to justify their implementation in a majority of CFD applications. Transition is critical to understanding the characteristics of the flow and can have drastic effects to the overall flow field. Aircraft design, performance and safety can all be improved if laminar-turbulent transition regions can be accurately simulated in an efficient manner.

Environmental concerns, fuel prices, regulations and economic volatility all contribute to the aerospace industry's drive for more efficient aircraft. This has led to continuous improvements though larger efficiencies have become more difficult in recent years as current aerospace technology is becoming mature. The International Council of Clean Transportation (ICCT) released a study demonstrating that reductions in fuel burn for new commercial aircraft since 2000 (seen in figure 1–1 [3]) have remained low. The major improvements to efficiency from the 1960s to the 1990s was the introduction of wide body planes such as the Boeing 747 in the 1970s and high-bypass turbofans in the 1980s. To further reduce the average fuel burn, future technologies such as geared turbo-fans, open rotors, biofuel and laminar flow control are anticipated to provide the next generation of efficient commercial aircraft.

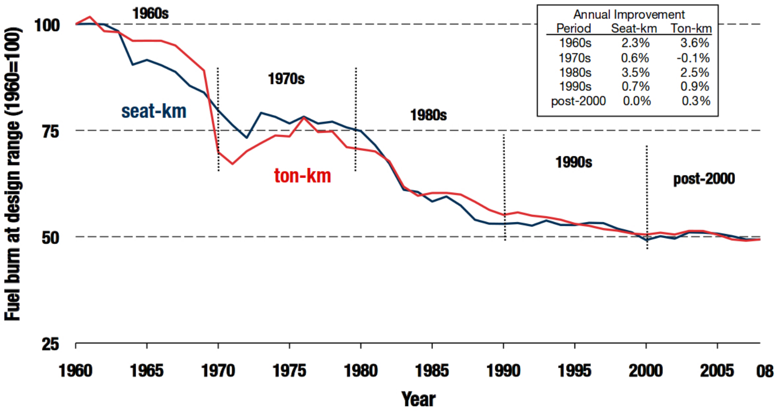

Figure 1–1: ICCT's study on the average fuel burn for new aircraft [3].

A growing concern for the industry is that as the current efficiency of aircraft is reaching a plateau, the number of airline passengers carried is growing. Airline traffic has been steadily increasing over the last 40 years [4], seen in figure 1–2, with a predicted doubling (as of 2011) to occur before 2040 [16]. This increase is mainly a result of the growth in the Asian/Pacific and Latin American markets. This puts the aerospace industry in the challenging situation of having to create aircraft with significantly large efficiencies to reduce the industry's overall environmental impact.

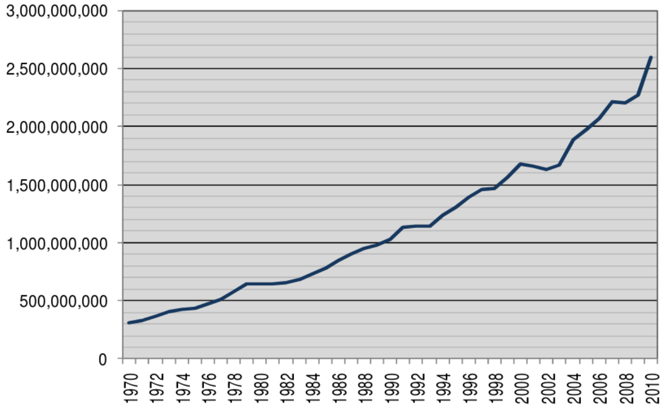

Figure 1–2: World Bank's historical world traffic in terms of passengers carried [4].

The American N+3 [17] and the European Clean Sky [18] governmental programs have been created to address this problem by increasing awareness on future environmental problems and to catalyse aeronautical innovation. The Clean Sky initiative aims to achieve the following by 2020 (using an aircraft made in 2000 as the base comparison):

- reduce CO_2 emissions by 50%
- reduce NO_x emissions by 80%
- reduce perceptible noise by 50%

The major rationale behind these targets and similar ones by the American N+3 program is to reduce the environmental damage of the aerospace industry and mitigate global warming. Airplanes release approximately 2-3% of all emitted CO_2 though their effect on the environment may be proportionally larger due to the high altitudes they fly at [19, 20]. Radical new technologies, designs and procedures are being explored to meet these aims such as blended wings, lifting bodies, formation flying and open rotor concepts. Unconventional concepts do not have significant, if any, experimental data and thus must be investigated computationally.

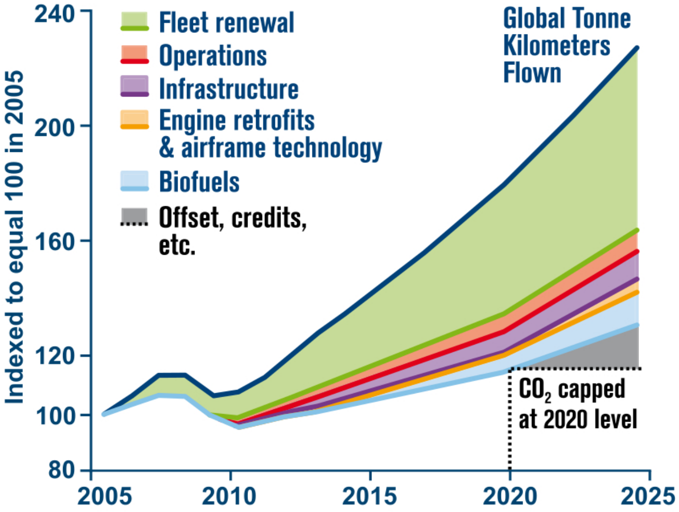

Figure 1–3: International Air Transport Association (IATA) index reporting on estimated global tonnes of fuel used and reduction strategies [5].

A few additional factors and technologies that can reduce pollution are shown in figure 1–3 where they are compared against the global tonnes of fuel used (standardized at the year 2005). New technologies introduced in fleet renewal are the main contributor for increased efficiency while additional methods such as biofuels and airline operations make relatively less contribution.

One of these novel methods within fleet renewal is to design for laminar flow. Laminar flow on the surface of an aircraft is usually desired to reduce the skin friction drag resulting in a lower required engine thrust and fuel burn. A 2009 study by the International Air Transport Association estimates that designing for laminar flow on an aircraft would reduce its fuel burn by 10-15% [5] while a study conducted by NASA estimates a fuel reduction of 25% [21]. Boeing is starting to use this concept and estimates that designing the engine nacelle on the 787 Dreamliner for laminar flow saves over 100,000 litres fuel/year [22].

Skin friction and heat transfer change dramatically between laminar and turbulent regions and an accurate transition model is needed to capture these effects. An error of just one drag count ($\Delta C_D = 0.0001$) decreases the payload by 200 lbs on a civil subsonic aircraft or by 1,000 lbs on a C-5 Galaxy [23, 24]. Note that one error in drag count is equal to 0.4% of the overall drag for the C-5 Galaxy.

1.2 Laminar, Transitional and Turbulent Flow

Fluid flow can be separated into three main regimes: laminar, transition and turbulent. A sketch of a typical boundary layer along a flat plate is shown in figure 1–4 which demonstrates these regions. Laminar flow is characterised by the relatively strong influence of viscous effects, low momentum convection and stability until a critical Reynolds number. Laminar flow tends to behave as it were a system of adjacent layers or lamellae which is where the term comes from [25]. Turbulent flow is characterised by the appearance of cascading eddies of various sizes, high momentum convection and chaotic fluctuations of the mean streamline velocity. Transitional flow is a combination of laminar and turbulent flow regimes [26]. The research presented in this thesis focuses on the breakdown of laminar to turbulent flow though relaminarization from turbulent to laminar is also possible.

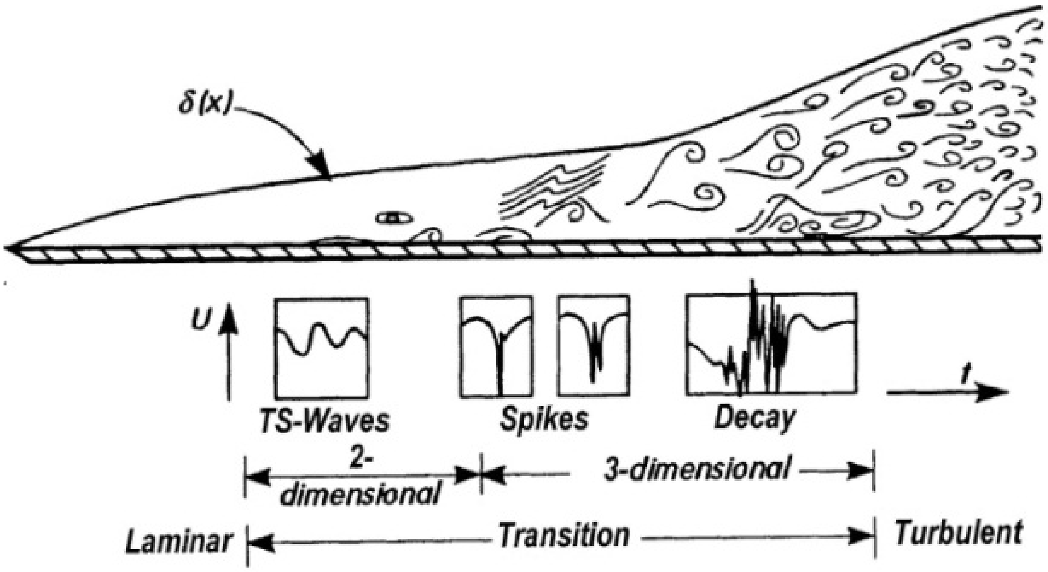

Figure 1–4: Sketch of the laminar, transition and turbulent flow on a flat plate [6].

There are three main design methods to extend the laminar region on an aircraft: active, passive and hybrid. Active methods use an additional system to modify the boundary layer velocity profile and usually burn additional fuel [27]. Some examples of active systems are boundary layer suction, plasma actuators and boundary layer cooling. Passive methods optimize the geometry to create favourable pressure gradients [28] to extend the transition point. Passive methods have the advantage of not adding additional weight, introducing no system complexity and do not burn additional fuel. Hybrid approaches are a combination of active and passive systems.

Starting in the 1930s when it was discovered that a favourable pressure gradient postpones transition, the design of natural laminar flow airfoils have been vigorously pursued. [29]. Natural laminar flow (NLF) airfoils are defined as profiles where over 30% of the wing is in the laminar regime by relying solely on a favourable pressure gradient [15, 29]. The NLF(1)-0416 airfoil that is discussed in section 3.2 was the result of NASA designing an airfoil with a specific pressure gradient profile, transition location limit and pitch characteristics.

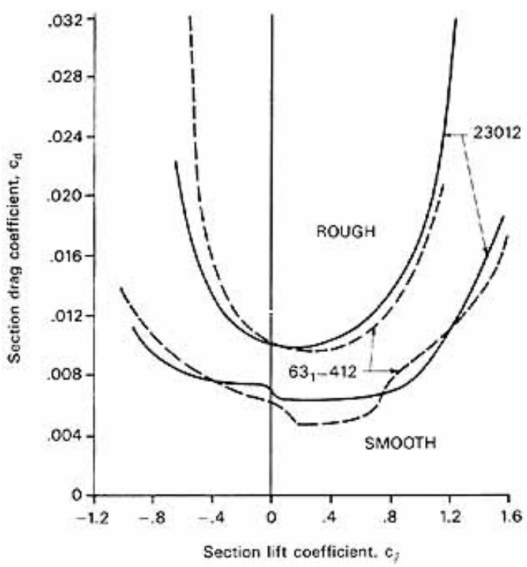

Figure 1–5: Drag polar of various NACA airfoils with smooth and rough leading edges [7].

NLF airfoils have plenty of advantages but their reliance on unstable laminar flow makes them susceptible to various catastrophic flight conditions. NLF airfoils are susceptible to stall, as laminar boundary layers are more likely to separate, making them highly dangerous at take-off and landing [30]. Surface roughness makes a large difference in overall drag (as can be seen in figure 1–5) and surface contaminants such as ice, uneven paint, rivets, bugs and dents all cause the boundary layer to transition much earlier than it would have without roughness. An aircraft section's premature transition into turbulence could cause a sudden loss of lift or increase of drag placing an aircraft into an unacceptably hazardous situation.

Another disadvantage is that NLF airfoils only have laminar flow over certain Reynolds numbers and angles of attack. The reliance on angle of attack can be seen in figure 1–5 where a "drag-bucket" is formed at low angles of attack for smooth airfoils. The drag-bucket is caused by a small regime where the flow is largely laminar. At higher angles of attack the boundary layer transitions to turbulence via separation or natural transition making the airfoil less optimized then one that is designed for turbulent flow in that flight condition.

1.3 Transition Mechanisms

A list of transition mechanisms that occur during external aerodynamic flows will be provided. The list is not exhaustive and for more information, such as re-laminarization or wake-induced separation, the reader is encouraged to refer to the following references [31, 32].

1.3.1 Natural Transition

Natural transition occurs in all flows where small disturbances, unable to be damped by viscous forces, are amplified and transformed into turbulence. These small disturbances can be caused by small freestream turbulence intensities, surface roughness or acoustic waves. When the freestream turbulence intensity is low (usually less than one percent [33]) and a certain Reynolds number has been met, Tollmien-Schlichting viscous waves form and destabilize the boundary layer.

Figures 1–6 and 1–7 show natural transition on a flat plate where the process breaks down into the three major phases. Receptivity in figure 1–6 or Zone (1) in

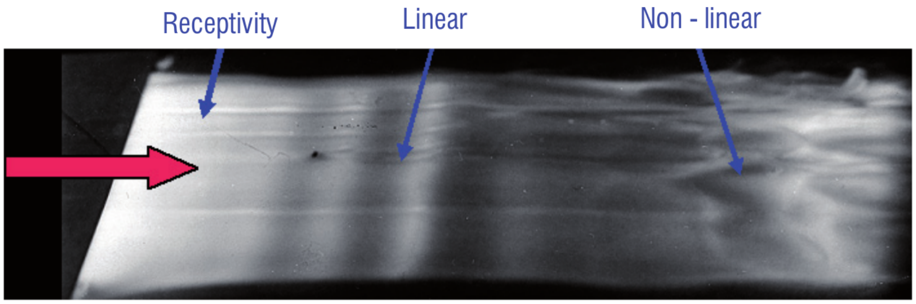

Figure 1–6: Experiment demonstrating natural transition in a water channel. Flow moves to the right as shown by the arrow [8].

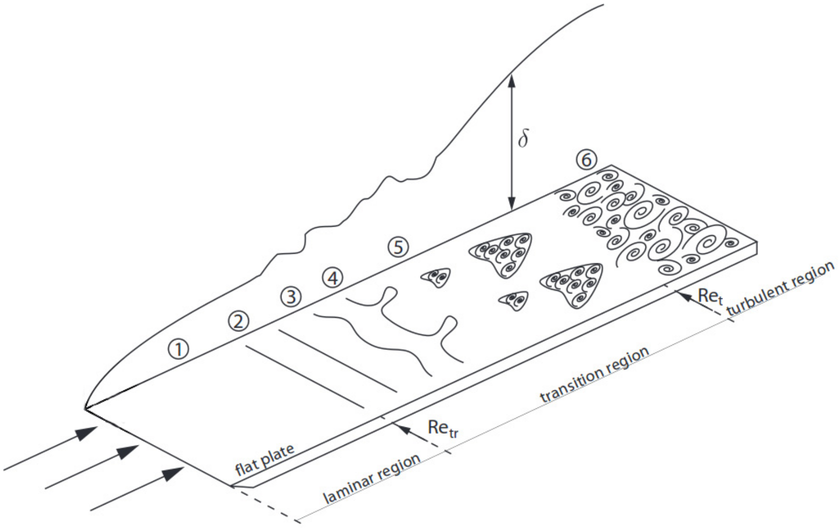

Figure 1–7: Sketch of natural transition along a flat plate with a uniform velocity [9].

figure 1–7 is a region where small disturbances, likely freestream turbulence or noise, enter the boundary layer. In the second zone, labelled Linear or Zones (2-5), the disturbances are amplified into periodic waves creating cascading three-dimensional structures that dramatically increase instability. Lastly, the laminar flow breaks down into turbulence as seen in the Non-linear region or Zone (6) in the above figures [6].

1.3.2 Crossflow Instabilities

Crossflow or spanwise flow is a three-dimensional effect where fluid travels perpendicular to the local inviscid flow velocity causing instability in the laminar boundary layer [10]. On aircraft with swept wings, the crossflow is parallel to the sweep and causes transition to occur much earlier then with just Tollmien-Schlichting waves. In backward swept wings the crossflow moves towards the tip while with a forward sweep it travels towards the wing root.

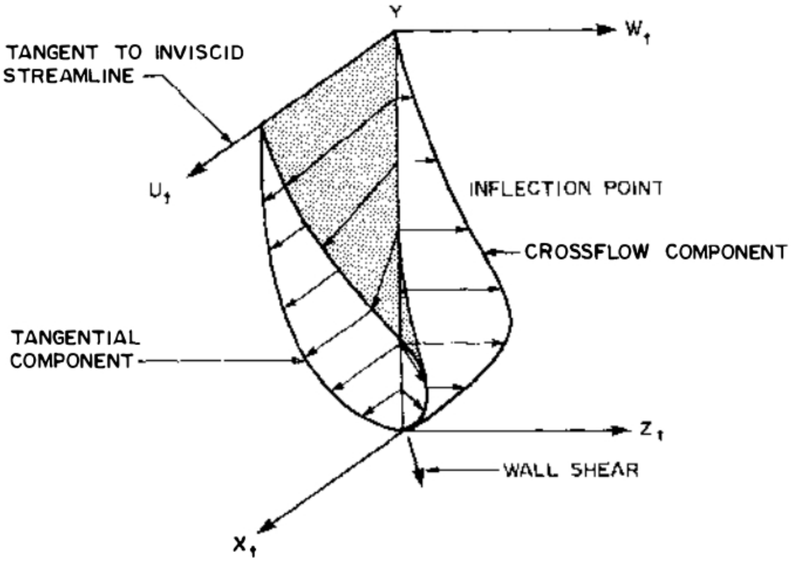

Figure 1–8: Schematic of velocity components within a swept-wing boundary layer illustrating the definition of the crossflow velocity [10].

The sweep of the leading edge and low momentum in the boundary layer causes a large deflection in the velocity resulting in a crossflow. A sketched velocity profile near the surface of a swept wing is illustrated in figure 1–8. The crossflow velocity is both zero at the wall and at the edge of the boundary layer while its maximum occurs approximately halfway through the boundary layer. The crossflow velocity profile has an inflection point which is known to be dynamically unstable [6]; this results in three-dimensional crossflow vortex structures that cause transition and are known as crossflow instabilities.

Figure 1–9: Oil flow visualization of crossflow and shock induced separation where the Mach is 0.85 [6].

A three-dimensional oil flow visualization of crossflow is shown in figure 1–9 and demonstrates how fluid will move towards the wing tip on negatively swept wings. There is also a shock induced separation that occurs approximately 50% along the span in figure 1–9. The effects of crossflow instabilities become a major limiting factor in designing aircraft and is particularly noticeable at lower Mach numbers and higher sweep angles. When the sweep angle is larger than 20 degrees there is practically no laminar flow on any wing of appreciable size due to the effects of crossflow instabilities [10]. The problem is compounded on NLF airfoils because the favourable pressure gradient used to stabilize streamwise instabilities destabilizes crossflow instabilities [34].

An example of this trade-off is illustrated through a concept aircraft developed jointly by NASA and the Boeing Aircraft Company. A study was performed based on experimental values and stability analysis to determine the effect of sweep on transition location [11]. As seen in figure 1–10, crossflow transition first occurs at 7 degrees sweep and quickly becomes the dominant transitional mechanism.

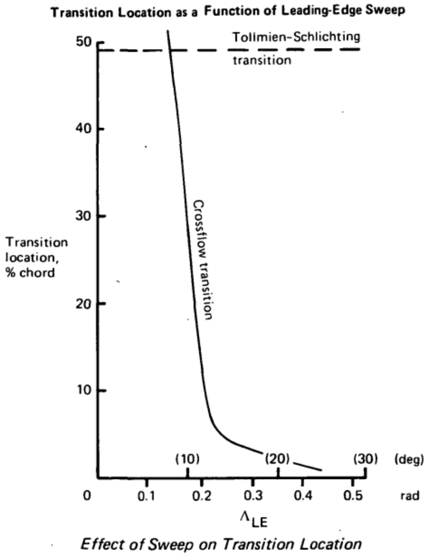

Figure 1–10: Wing sweep versus transition location of concept aircraft by NASA [11].

1.3.3 Bypass Transition

Bypass transition occurs when the primary stages of natural transition are bypassed when large freestream disturbances directly create turbulent spots within a boundary layer [33]. These disturbances can be caused by large turbulent freestream intensities ($> 1\%$), surface roughness or when turbulent flow is injected into the main flow [35]. The main mechanism for transition in turbomachinery applications is bypass transition; high freestream turbulence is generated by upstream blades and is imposed on the boundary layer of downwind blades causing transition [36].

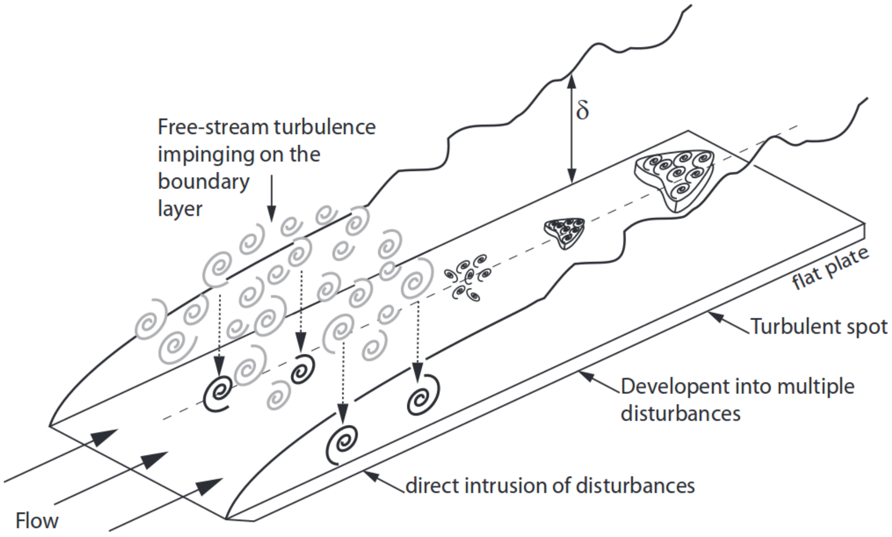

Figure 1–11: Sketch of bypass transition along a flat plate with a uniform velocity [9].

Figure 1–11 shows a sketch of bypass transition where disturbances with a certain size and strength directly intrude into the boundary layer. Other bypass modes also exist such as when long elongated structures with varying velocity profiles appear in the boundary layer due to high freestream intensity then subsequently cascade and cause transition [9].

1.3.4 Separated Flow Transition

Laminar to turbulent transition can also be triggered when a laminar boundary layer separates and the resulting mixing causes transition [33]. Transition may start to occur in the shear layer because of an inviscid instability mechanism that may include Tollmien-Schlichting waves [31]. In cases with a large adverse pressure gradient, reverse flow occurs and an inflection point is present in the velocity profile which triggers transition [31] as it is unstable. Separated flow transition may be desirable as a forward laminar separation/turbulent-reattachment bubble may be more inclined to attach to the airfoil preventing a "long" separation bubble. The most common occurrence of this transition mechanism is when a wing has stalled such as the NACA4421 shown in figure 1–12.

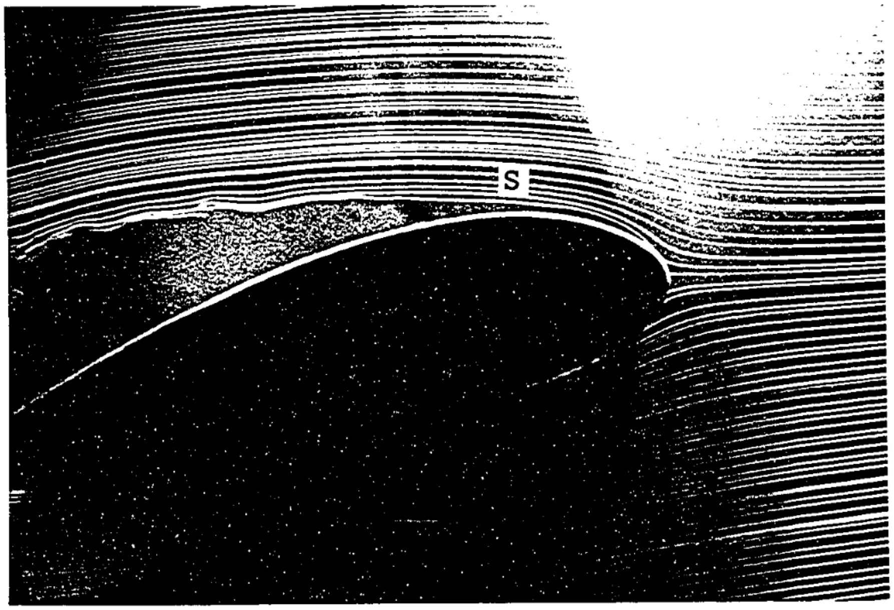

Figure 1–12: Laminar induced separation of a NACA4421 airfoil at α=16.0 and Reynold number of 6800. The separation occurs at approximately 15% along the chord [12].

The rapid transition from laminar to turbulent flow due to the interaction between a shock wave and boundary-layer is not completely understood but it is conceptualized that the process is similar to separated flow transition [37].

1.4 Transition Modelling

Ever since Osborne Reynolds' experiment demonstrating the breakdown of laminar to turbulent flow, there has been considerable research into the mechanisms of transition [6, 9, 33, 35, 36, 38, 39, 40]. The complex and not completely understood physical breakdown of a flow causes difficulty in formulating a transition model based on first-principles. Transition involves many non-linear processes involving a wide range of scales. It is very sensitive to initial conditions and geometry making it difficult to predict the transition region and length *a priori*. Each mechanism for transition is governed by different physical forces making a simple transition model that encompasses them all unlikely. Transition models are particularly difficult to implement in a typical Reynolds-averaged Navier-Stokes (RANS) environment as the time/mass averaging filters out linear growths.

A non-exhaustive list of important transition models are presented in the following subsection though a more detailed and enumerated list can be found in Pasquale et al. [41].

1.4.1 Direct Numerical Simulations

Direct numerical simulations (DNS) are suitable for the prediction of transition regions. However, their required computational resources, coupled with the challenges of specifying far-field conditions, make them currently impractical for aerospace applications [41, 42]. Solving a fluid flow using DNS is the ideal method for CFD as it is derived from first-principles and requires no closure equations. To properly resolve the fluid flow, DNS simulations require a minimum grid size that is fine enough to capture the smallest turbulence scales. The order of magnitude of the minimum grid size scales as $Re^{9/5}$ [43] and since commercial aircraft regularly fly at Reynolds numbers higher than 10 million, this makes DNS infeasible within the foreseeable future. A study by Spalart estimates that a grid size of 10^{16} and more than 10^{7} time steps are needed for industrial applications; thus Spalart estimates that supercomputers will not be powerful enough to solve industrial applications using DNS until 2080 [44].

1.4.2 Large Eddy Simulations

Large eddy simulations or LES directly computes the large scales of a fluid flow but models the small subgrid-scales using an eddy viscosity approach. LES simulations consequently employ coarser grids compared to DNS since the expensive small scales are eliminated; acting similar to a low-pass filter for the flow. The small subgrid-scales are modelled using functions based on experimental values proposed by Smagorinsky [45]. When modelling transition using LES, the transition region is sensitive to the Smagorinsky constant and a constant value for all simulations has yet to be found [41, 46]. Transition locations comparing LES and DNS simulations show good results yet Michelassi et al. [47] have found discrepancies between LES and DNS, highlighting that more work is needed for LES to properly capture transition. A study by Spalart estimates LES grid sizes for industrial application will be in the order of 10^{11} with supercomputers powerful enough to solve them entering the market around 2045 [44].

1.4.3 e^n Method / Stability Theory Approach

The stability theory approach predicts transition by tracking the behaviour of small disturbances to determine if they grow into turbulence. An example of an equation solved with this approach is equation (1.1), otherwise known as the Orr-Sommerfeld equation, which models the growth of a single oscillation in a two-dimensional, incompressible, unsteady flow [48, 49]. Equation (1.1) can be reduced to an eigenvalue problem where eigenvalues determine whether a disturbance grows or diminishes [41].

$$(U-c)(\phi''-\alpha^2\phi)-U''\phi=\frac{-i}{\alpha R}(\phi^{(4)}-2\alpha^2\phi''+\alpha^4\phi) \tag{1.1}$$

Instead of tracking all disturbances, a popular stability approach is to use the e^n method which looks at the most unstable amplification rate and correlates it with the onset of transition. The velocity and temperature profiles are first calculated, then the local growth rates of the unstable waves are calculated, finally the local growth rates are integrated along the streamline to see if they exceed a certain predetermined value based on n. The e^n method can be represented in equation (1.2) though empirical data is needed for each testcase as n is not a universal constant [50, 51].

$$\frac{A}{A_0}=\exp\left[\int_{x_0}^{x}-\alpha dx\right]=\exp[n] \tag{1.2}$$

This method works well for predicting natural transition on two-dimensional grids but its implementation and accuracy is problematic when extended to three-dimensions, parallel applications or unstructured grids. The challenges of tracking disturbances along streamlines and lack of accuracy of most solvers to evaluate the stability equation preclude universal usage of this model. It also does not take account of non-linear effects such as bypass transition, roughness, separation and length of transition.

1.4.4 Empirical Correlations / Intermittency Transport Method

To simulate transition with complex flows, a semi-empirical approach can be used that blends together laminar and turbulent regions based on experimental data. A parameter called the intermittency or γ is used to represent the percentage of time a flow is turbulent. Turbulence is usually controlled by using γ as a scaling factor on the eddy viscosity in a RANS environment. An example equation of this blending function can be found in equation (1.3) [52]. These methods are often used for bypass and separation induced transition.

$$\frac{\partial \gamma}{\partial t}+\frac{\partial \rho u_j \gamma}{\partial x_j} = (1-\gamma)\left[(1-F)C_0\rho\sqrt{u_k u_k}\beta(s) + F\left(\frac{C_1\gamma}{\kappa}\tau_{ij}\frac{\partial u_i}{\partial x_j} - C_2\gamma\rho\frac{\kappa^{3/2}}{\epsilon}\frac{u_i}{(u_k u_k)^{1/2}}\frac{\partial u_i}{\partial x_j}\frac{\partial \gamma}{\partial x_j}\right)\right] \\ + C_3\rho\frac{\kappa^2}{\epsilon}\frac{\partial \gamma}{\partial x_j}\frac{\partial \gamma}{\partial x_j} + \frac{\partial}{\partial x_j}\left(\left[(1-\gamma)\gamma\sigma_{\gamma t}\mu + (1-\gamma)\sigma_{\gamma t}\mu_t\right]\frac{\partial \gamma}{\partial x_j}\right) \quad (1.3)$$

Though these methods have found some success, a major issue is their use of a non-local formulation. This approach requires information inside the boundary layer as well as knowledge of flow conditions outside the boundary layer and at freestream. These methods tend to work well in turbomachinery environments but they still require calibration for each testcase and their formulation precludes their efficient integration into modern CFD codes [41].

1.4.5 The Intermittency and Vorticity Reynolds Number Approach

A transition model consisting of only local variables has been formulated by Menter et al. [53] and is based on a two-equation transport model with the production of intermittency correlated to the local vorticity Reynolds number. The first equation solves for the intermittency, tracking the local levels of turbulence throughout the domain. The second equation solves for the transition onset Reynolds number which correlates non-local effects such as adverse pressure gradient to local variables. This model is called the $\gamma - \overline{Re_{\theta t}}$ transition model and has the advantage of being compatible with modern CFD approaches, massive parallel executions, unstructured grid topologies and accounts for various complex transition phenomena. The $\gamma - \overline{Re_{\theta t}}$ model increases the run time of a RANS simulation with a two-equation turbulence model by approximately 20% [31] making it economically viable for the majority of industrial applications already being simulated. This model does not attempt to simulate the underlying physical processes behind transition but uses experimental data to correlate and predict relevant transitional parameters. These correlation functions are based on curve fitting relationships from a limited experimental data set and further research is required to ensure they are optimized for a wide range of flow conditions. Additionally, some correlations, most notably crossflow instabilities, are not included in the model. Nevertheless, this approach holds great promise to allow first order effects of transition to be introduced into a RANS environment [31]. As the $\gamma - \overline{Re_{\theta t}}$ transition model and its three-dimensional applications will be the focus of this thesis, a more detailed description of this model will be provided in section 2.4.

1.5 Thesis Outline

The motivation behind this research was to determine the accuracy and robustness of the $\gamma - \overline{Re_{\theta t}}$ transition model in three-dimensions. In chapter 1, the importance of transition was discussed along with various transition mechanisms and models. Chapter 2 goes into depth about the governing equations used in this research. Section 2.1 to 2.3 introduces the Navier-Stokes, RANS and turbulence equations. A detailed explanation of the $\gamma - \overline{Re_{\theta t}}$ transition model is given in section 2.4. The modifications to the model from Menter's original introduction is provided in section 2.5. The numerical results for the NACA0012, NLF(1)-0416 and DLR-F5 are presented in chapter 3. Two quasi three-dimensional airfoils were used for validation, section 3.1 for the NACA0012 and section 3.2 for the NLF(1)-0416, while the three-dimensional DLR-F5 wing is presented in section 3.3. Chapter 4 discusses the conclusions found during this research as well as proposes future work to further increase the accuracy, robustness and applicability of the $\gamma - \overline{Re_{\theta t}}$ transition model.

1.6 Author's Contributions

The author extended and implemented the modified $k - \omega$ SST turbulence and $\gamma - \overline{Re_{\theta t}}$ transition model into three dimensions and incorporated them into a three-dimensional RANS solver. A circulation correction and preconditioner was also added to the RANS solver. Two quasi two-dimensional airfoils were validated and compared with both experimental data and other transition models. A fully three-dimensional grid was refined from surface geometry, simulated and compared against experimental data.

CHAPTER 2
Computational Fluid Modelling

This chapter summarizes the relevant governing equations and mathematical models used within this research. A brief explanation in section 2.1 for the Navier-Stokes equations will be made and then in section 2.2 the RANS and their assumptions will be described. In section 2.3, the $k-\omega$ Shear Stress Transport(SST) turbulence model will be summarized. The $\gamma - \overline{Re_{\theta t}}$ transition model will be explored and described in depth in section 2.4. Section 2.5 details the various modifications made to the turbulence and transition models and their rationale. The implementation of the transition model into the turbulence model will be discussed in section 2.6. A summary of the mathematical methods and convergence acceleration techniques will be completed in section 2.7.

2.1 Navier-Stokes Equations

Applying the equations of Navier-Stokes [54, 55], mass and energy to a fluid element in a continuum results in a set of partial non-linear equations that describe stationary and moving fluids. When combined with the relevant thermodynamic relation and solved, they determine the fluid properties such as density, velocity, specific energy, pressure and entropy at any point in the fluid. Taking the differential conservative form of the three-dimensional Navier-Stokes equations in Cartesian form with Einstein notation where $i = 1, 2, 3$ yields

$$\frac{\partial \vec{w}}{\partial t} + \frac{\partial \vec{f_i}}{\partial x_i} - \frac{\partial \vec{f}_{vi}}{\partial x_i} = \vec{q_b} \quad \text{in } \mathbb{D}, \tag{2.1}$$

with

$$\vec{w} = \begin{pmatrix} \rho \\ \rho u_1 \\ \rho u_2 \\ \rho u_3 \\ \rho E \end{pmatrix}, \vec{f_i} = \begin{pmatrix} \rho u_i \\ \rho u_1 u_i + p\delta_{i1} \\ \rho u_2 u_i + p\delta_{i2} \\ \rho u_3 u_i + p\delta_{i3} \\ \rho E u_i + p u_i \end{pmatrix}, \vec{f}_{vi} = \begin{pmatrix} 0 \\ \tau_{ij}\delta_{j1} \\ \tau_{ij}\delta_{j2} \\ \tau_{ij}\delta_{j3} \\ u_j \tau_{ij} + k\frac{\partial T}{\partial x_i} \end{pmatrix}, \tag{2.2}$$

where x_i and t are the Cartesian coordinates and time respectively. $\mathbb{D}$ is the domain under consideration, ρ is the density, E is the specific total energy, δ_{ij} is the Kronecker delta function, $\vec{f_i}$ is the inviscid flux vector, $\vec{f}_{vi}$ is the viscous flux vector, $\vec{q_b}$ is the potential body forces and p is the pressure. In all the testcases being examined in this research the potential body forces are zero.

Air, the working fluid for the aerodynamic testcases presented in this thesis, acts as a Newtonian fluid resulting in the following definition of viscous shear

$$\tau_{ij} = \mu \left[\frac{\partial u_i}{\partial x_j} + \frac{\partial u_j}{\partial x_i} \right] + \lambda \left[\frac{\partial u_k}{\partial x_k} \right] \delta_{ij}. \tag{2.3}$$

The second viscosity coefficient is replaced with $\lambda = -\frac{2\mu}{3}$ from Stokes' hypothesis.

The Navier-Stokes equations require an additional thermodynamic relation that relates temperature, density and pressure. Within this research only aerodynamic cases will be considered that use air as a working fluid such that the ideal gas law (equation 2.4) is valid. Air, at the altitudes and Mach numbers being investigated, acts as a calorically perfect gas where the ideal gas law can be applied and takes the form

$$p = \rho R_{air} T, \quad R_{air} = 287.058 \frac{\mathrm{J}}{\mathrm{kg} \cdot \mathrm{K}}. \tag{2.4}$$

Sutherland's law, provided below with the relevant air constants, is used to relate the viscosity to the temperature.

$$\mu = C_{1air} \frac{T^{3/2}}{T + C_{2air}}, \quad C_{1air} = 1.458 \times 10^{-6} \frac{\mathrm{kg}}{\mathrm{m} \cdot \mathrm{s}\sqrt{\mathrm{K}}}, \quad C_{2air} = 110.4K. \tag{2.5}$$

The thermal conductivity coefficient k is from Fourier's law of heat conduction and is calculated by

$$k = \frac{c_p \mu}{Pr},$$

where Pr is the Prandtl number, c_p is the specific heat at constant pressure and γ is the ratio of specific heats.

The specific heat at constant pressure is calculated by

$$c_p = \frac{\gamma R}{\gamma - 1},$$

with $\gamma_{air} = 1.4$.

For additional information on the Navier-Stokes equations please refer to [56, 57, 58].

2.1.1 Farfield Flow Conditions

Farfield boundary conditions are set using Riemann invariants. Waves propagating outside the domain are extrapolated while waves entering the domain are calculated using freestream conditions. A more detailed description can be found in Jameson et al. [59].

A circulation correction to the far-field boundary condition as noted in equation (2.6) is employed to increase accuracy [60]. Equation (2.6) is in Cartesian form with Γ being the circulation and l the half-span. The parameters A, B, C and β are functions of x, y, z and l.

$$
\begin{aligned}
u_\infty^* &= u_\infty + \frac{\Gamma\beta^2}{2\pi}A \\
v_\infty^* &= v_\infty - \frac{\Gamma}{2\pi}\left[\frac{z+l}{(z+l)^2+y^2}B - \frac{z-l}{(z-l)^2+y^2}C + \frac{x\beta^2}{x^2+y^2\beta^2}A\right] \\
w_\infty^* &= w_\infty + \frac{\Gamma}{2\pi}\left[\frac{y}{(z+l)^2+y^2}B - \frac{y}{(z-l)^2+y^2}C\right].
\end{aligned}
\tag{2.6}
$$

2.1.2 Flow Wall Boundaries

The flow wall boundary conditions of zero flux through the wall and no slip are applied on the wall surface. They are defined as

$$(u_i \cdot \hat{n}_i)_{wall} = 0, \quad (u_i \cdot \hat{t}_i)_{wall} = 0,$$

where $\hat{n}_i$ is the unit normal vector at the wall and $\hat{t}_i$ is the unit tangent vector.

2.2 Reynolds-averaged Navier-Stokes (RANS) Equations

Reynolds decomposition is applied to the complete Navier-Stokes equations such that each flow variable is comprised of a mean and fluctuating component. The resulting equations are called the Reynolds-averaged Navier-Stokes equations or RANS equations. The averaging of the Navier-Stokes equations is done such that the turbulent fluctuations can be isolated and a separate turbulence model can be used to approximate these fluctuations. More information on the derivation and averaging process can be found in Blazek [60] and Wilcox [61].

The RANS equations introduce additional non-physical terms caused by the averaging process and additional closure equations are needed. The Boussinesq approximation [62], which proposes that the Reynolds stress tensor is proportional to the mean strain rate tensor, replaces these additional terms by an eddy viscosity. The viscosity is separated into a laminar and eddy viscosity such that total viscosity is equal to

$$\mu = \mu + \mu_t. \tag{2.7}$$

The thermal conductivity is replaced with

$$k = k + k_t = c_p \left(\frac{\mu}{Pr} + \frac{\mu_t}{Pr_t} \right), \tag{2.8}$$

where Pr_t is the turbulent Prandtl number. The laminar and turbulent Prandtl are used to calculate the heat conduction from the viscosity are are taken to be a constant value of 0.72 and 0.9 respectively [63].

2.3 $k - \omega$ Shear Stress Transport Turbulence Model

The $k - \omega$ Shear Stress Transport ($k - \omega$ SST) turbulence model introduced by Menter [64] is employed to calculate the eddy viscosity and act as a closure model for the RANS equations with the Boussinesq approximation. The model is in the same form as originally presented by Menter [64] except an ambient term is added in equation (2.9) and (2.10) to cancel out the numerical dissipation present in external flows [65]. The $k-\omega$ SST model blends the $k-\epsilon$ proposed by Jones and Launder [66] with the $k-\omega$ developed by Wilcox [67] so that the flaws in each model are mitigated by the other. The $k-\epsilon$ model is used in the wake and freestream shear regions and gradually switches to the $k-\omega$ model in the boundary layer. Menter blends these models as the $k-\epsilon$ is not sensitive enough to adverse pressure gradients and is numerically stiff in the boundary layer while the $k-\omega$ is too dependent on freestream conditions.

The two transport equations solved for the $k-\omega$ SST turbulence model are equation (2.9) for the turbulent kinetic energy (k)

$$\frac{\partial(\rho k)}{\partial t}+\frac{\partial(\rho u_j k)}{\partial x_j}=P_\tau-\beta^*\rho\omega k+\frac{\partial}{\partial x_j}\left[(\mu+\sigma_k\mu_t)\frac{\partial k}{\partial x_j}\right]+\beta^*\rho\omega_\infty k_\infty, \tag{2.9}$$

and equation (2.10) for the specific turbulent dissipation rate (ω)

$$\frac{\partial(\rho\omega)}{\partial t}+\frac{\partial(\rho u_j\omega)}{\partial x_j}=\frac{\gamma}{\nu_t}P_\tau-\beta\rho\omega^2+\frac{\partial}{\partial x_j}\left[\left(\mu+\sigma_\omega\mu_t\right)\frac{\partial\omega}{\partial x_j}\right]+2(1-F_1)\frac{\rho\sigma_{\omega 2}}{\omega}\frac{\partial k}{\partial x_j}\frac{\partial\omega}{\partial x_j}+\beta\rho\omega_\infty^2, \tag{2.10}$$

where

$$P_\tau=\tau_{ij}\frac{\partial u_i}{\partial x_j}, \tag{2.11}$$

and $\nu_t=\frac{\mu_t}{\rho}$. There exists many variations of the $k-\omega$ SST turbulence model but most have a production limiter for the turbulent kinetic energy [68]

$$P_\tau=\min(P_\tau,20\beta^*\rho\omega k). \tag{2.12}$$

Since the $k - \omega$ SST turbulence model is a blend of two models, the constants are blended such that each constant can be calculated by equation (2.13)

$$\phi = F_1\phi_1 + (1 - F_1)\phi_1, \tag{2.13}$$

with constants equal to

$$\gamma_1 = \frac{\beta_1}{\beta^*} - \frac{\sigma_{\omega 1}\kappa^2}{\sqrt{\beta^*}}, \quad \gamma_2 = \frac{\beta_2}{\beta^*} - \frac{\sigma_{\omega 2}\kappa^2}{\sqrt{\beta^*}}$$

$$\sigma_{k1} = 0.85, \quad \sigma_{\omega 1} = 0.5, \quad \sigma_{k2} = 1.0, \quad \sigma_{\omega 2} = 0.856, \quad \beta_1 = 0.075$$

$$\beta_2 = 0.0828, \quad a_1 = 0.31, \quad \beta^* = 0.09, \quad \kappa = 0.41,$$

where F_1 is a hyperbolic blending function that blends the $k - \epsilon$ and $k - \omega$ turbulence models. F_1 is formulated such that for a large portion of the boundary layer (approximately $\frac{\delta}{2}$) F_1 is equal to 1.0 but tends to zero at the edge of the boundary layer to ensure the freestream independence of the $k - \epsilon$ model. The derivation of F_1 is

$$F_1 = \tanh(arg_1^4), \tag{2.14}$$

with argument

$$arg_1 = \min\left[\max\left(\frac{\sqrt{k}}{\beta^*\omega d}, \frac{500\nu}{d^2\omega}\right), \frac{4\rho\sigma_{\omega 2}k}{CD_{k\omega}d^2}\right], \tag{2.15}$$

with d equalling the distance to the nearest wall, $\nu = \frac{\mu}{\rho}$ and $CD_{k\omega}$ is the cross diffusion term defined as

$$CD_{k\omega} = \max\left(2\rho\sigma_{\omega 2}\frac{1}{\omega}\frac{\partial k}{\partial x_j}\frac{\partial \omega}{\partial x_j}, 10^{-20}\right). \tag{2.16}$$

In addition to blending the $k-\omega$ and $k-\epsilon$ turbulent models, the $k-\omega$ SST model accounts for the transport of the principle turbulent stresses. Equation (2.17) uses Bradshaw's assumption which states that the shear-stress in a boundary layer is proportional to the turbulent kinetic energy [64]. The final result is an eddy viscosity term (μ_t) that accounts for the turbulent fluctuations in the RANS equations and is defined as

$$\mu_t = \frac{\rho a_1 k}{\max(a_1\omega, \Omega F_2)}, \tag{2.17}$$

where a_1 is used to scale the eddy viscosity, Ω is the vorticity magnitude and F_2 acts as a blending function with the definition

$$F_2 = \tanh(arg_2^2), \tag{2.18}$$

with argument

$$arg_2 = \max\left(2\frac{\sqrt{k}}{\beta^*\omega d}, \frac{500\nu}{\omega d^2}\right). \tag{2.19}$$

2.3.1 Farfield Turbulence Conditions

The recommended freestream turbulence variables k_∞ and ω_∞ are equal to [69]

$$k_\infty = 10^{-6}U_\infty^2 \quad \text{and} \quad \omega_\infty = \frac{5U_\infty}{L}. \tag{2.20}$$

2.3.2 Turbulent Wall Boundaries

The wall boundaries for the turbulence model are [64]:

$$k_{\text{wall}} = 0 \quad \text{and} \quad \omega_{\text{wall}} = \frac{60\nu}{\beta_1 d^2}. \tag{2.21}$$

2.4 Transition Modelling

The $\gamma - \overline{Re_{\theta t}}$ transition model is a two equation transport model that uses the vorticity Reynolds number (defined in equation 2.26) and various correlations to simulate a wide range of transition mechanisms. The first transport equation solves for the intermittency, represented by the symbol γ, which corresponds to the amount of time the fluid is turbulent. The second transport equation solves the local transition onset momentum-thickness Reynolds number or $\overline{Re_{\theta t}}$ which accounts for the non-local effects such as the freestream turbulence intensity or the pressure gradient outside the boundary layer. A complete description of the $\gamma - \overline{Re_{\theta t}}$ transition model can be found in the works of Menter et al. [13, 31, 70].

The form of the $\gamma - \overline{Re_{\theta t}}$ transition model with the temporal, advection and diffusion terms are similar to the two equation transport turbulence models such as the $k - \omega$ [69] or $k - \epsilon$ [71] models. Unlike these turbulence models, the transition model does not attempt to model the underlying physics behind the complex nature of transition but uses the following items to correlate local variables with the non-local properties of transition:

- the production of intermittency is triggered by the vorticity Reynolds number which can be related to the momentum thickness Reynolds number by the analytical Blasius solution. The physical assumption is that laminar flow will transition into turbulence when the local velocity shear in a boundary layer is both sufficiently large and far enough away from a wall [40, 53].
- curve fitting correlations based on various experiments that diffuse into the boundary layer to take into account non-local parameters [31, 39]. $\overline{Re_{\theta t}}$ is set

to equal experimental correlations outside the boundary layer and diffuses into the boundary layer to create local variables to trigger transition.

- the solution to the transition model results in an effective intermittency value that scales the production of the turbulent kinetic energy [31].

The two transport equations solved for the $\gamma - \overline{Re_{\theta t}}$ transition model are equation (2.22) for the intermittency (γ)

$$\frac{\partial(\rho\gamma)}{\partial t} + \frac{\partial(\rho u_j \gamma)}{\partial x_j} = P_\gamma - E_\gamma + \frac{\partial}{\partial x_j}\left[\left(\mu + \frac{\mu_t}{\sigma_f}\right)\frac{\partial\gamma}{\partial x_j}\right], \tag{2.22}$$

and equation (2.23) for the local transition onset momentum-thickness Reynolds number ($\overline{Re_{\theta t}}$)

$$\frac{\partial(\rho\overline{Re_{\theta t}})}{\partial t} + \frac{\partial(\rho u_j \overline{Re_{\theta t}})}{\partial x_j} = P_{\theta t} + \frac{\partial}{\partial x_j}\left[\sigma_{\theta t}\left(\mu + \mu_t\right)\frac{\partial\overline{Re_{\theta t}}}{\partial x_j}\right]. \tag{2.23}$$

The production of intermittency is provided in equation (2.24) and will be explained in detail in section 2.6.

$$P_\gamma = F_{Length} c_{a1} \rho S [\gamma F_{onset}]^{0.5} (1.0 - c_{e1}\gamma). \tag{2.24}$$

F_{onset} is a trigger function that is zero but switches to a positive number when the vorticity Reynolds number and various other criteria exceed certain predetermined values. F_{onset} is defined as

$$F_{onset} = \max(F_{onset2} - F_{onset3}, 0), \tag{2.25}$$

with Re_v representing the vorticity Reynolds number (though it is formulated using the strain rate), F_{onset1} correlating the vorticity Reynolds number with the critical

Reynolds number of the Blasius boundary layer, Re_c or critical Reynolds number which will be described in equation (2.35), S is the strain rate and d is the closest distance to the wall. F_{onset2} is formulated to rapidly shift from zero to a positive number and F_{onset3} is introduced to help prevent stalled transition. The following variables are defined as

$$Re_v = \frac{\rho d^2 S}{\mu} \tag{2.26}$$

$$F_{onset1} = \frac{Re_v}{2.193 Re_{\theta c}} \quad , \quad F_{onset2} = \min[\max(F_{onset1}, F^4_{onset1}), 2.0] \tag{2.27}$$

$$R_T = \frac{\rho k}{\mu \omega} \quad , \quad F_{onset3} = \max\left(1 - \left(\frac{R_T}{2.5}\right)^3, 0\right). \tag{2.28}$$

Another important parameter in the production of intermittency is F_{Length} which determines the length of transition and is governed by various experimental data [13]. F_{Length} is defined as

$$F_{Length} = \begin{cases} 398.189 \cdot 10^{-1} - 119.270 \cdot 10^{-4}\overline{Re_{\theta t}} - 132.567 \cdot 10^{-6}\overline{Re_{\theta t}}^2, & \overline{Re_{\theta t}} < 400 \\ 263.404 - 123.939 \cdot 10^{-2}\overline{Re_{\theta t}} + 194.548 \cdot 10^{-5}\overline{Re_{\theta t}}^2 & \\ -101.695 \cdot 10^{-8}\overline{Re_{\theta t}}^3, & 400 \leq \overline{Re_{\theta t}} < 596 \\ 0.5 - (\overline{Re_{\theta t}} - 596.0) \cdot 3.0 \cdot 10^{-4}, & 596 \leq \overline{Re_{\theta t}} < 1200 \\ 0.3188, & 1200 \leq \overline{Re_{\theta t}} \end{cases} \tag{2.29}$$

where it is further modified to smooth the skin friction by limiting the maximum length of transition in the viscous sublayer such that

$$F_{Length} = F_{Length}(1.0 - F_{sublayer}) + 40.0 F_{sublayer}, \tag{2.30}$$

where

$$F_{sublayer} = e^{-\left(\frac{R_\omega}{0.4}\right)^2} \quad \text{and} \quad R_\omega = \frac{\rho d^2 \omega}{500\mu}. \tag{2.31}$$

The destruction/relaminarization term is provided below:

$$E_\gamma = c_{a2}\rho\Omega F_{turb}(c_{e2}\gamma - 1.0), \tag{2.32}$$

with Ω equalling to the vorticity magnitude. F_{turb} is used to disable the destruction outside of a laminar boundary layer or in the viscous sublayer and is defined as

$$F_{turb} = e^{-\left(\frac{R_T}{4}\right)^4}, \tag{2.33}$$

with the following constants

$$c_{e1} = 1.0, \quad c_{a1} = 2.0, \quad \sigma_f = 1.0, \quad c_{e2} = 50, \quad c_{a2} = 0.006. \tag{2.34}$$

c_{e1} limits the production of intermittency (equation 2.24) such that the maximum intermittency is 1.0 while c_{e2} limits the minimum intermittency to 0.02. The additional coefficients are chosen to best represent flat plate experiments.

The critical Reynolds number or $Re_{\theta c}$ is where intermittency first starts to increase, occurring before $Re_{\theta t}$, and is defined as

$$Re_{\theta c} = \begin{cases} \overline{Re_{\theta t}} - 396.035 \cdot 10^{-2} - 120.656 \cdot 10^{-4}\overline{Re_{\theta t}} + 868.230 \cdot 10^{-6}\overline{Re_{\theta t}}^2 & \\ -696.506 \cdot 10^{-9}\overline{Re_{\theta t}}^3 + 174.105 \cdot 10^{-12}\overline{Re_{\theta t}}^4, & \overline{Re_{\theta t}} \leq 1870 \\ \overline{Re_{\theta t}} + (593.11 - (\overline{Re_{\theta t}} - 1870.0) \cdot 0.482). & \overline{Re_{\theta t}} > 1870 \end{cases} \tag{2.35}$$

The production of the local transition onset momentum-thickness Reynolds number is formulated such that no production or destruction occurs outside the boundary layer and $\overline{Re_{\theta t}}$ equals the values set from experiments. The production of $\overline{Re_{\theta t}}$ equals to

$$P_{\theta t} = c_{\theta t}\frac{\rho}{t}(Re_{\theta t} - \overline{Re_{\theta t}})(1.0 - F_{\theta t}), \tag{2.36}$$

where t is a term used to non-dimensionalize the production of $\overline{Re_{\theta t}}$ and $|u|$ is the velocity magnitude

$$t = \frac{500\mu}{\rho|u|^2}. \tag{2.37}$$

A blending function ($F_{\theta t}$) is used which is equal to zero inside the boundary layer and 1.0 outside so that the local transition onset momentum-thickness Reynolds number ($\overline{Re_{\theta t}}$) diffuses into the boundary layer. $F_{\theta t}$ is defined as

$$F_{\theta t} = \min\left[\max\left\{F_{wake} \cdot e^{-\left(\frac{d}{\delta}\right)^4}, 1.0 - \left(\frac{\gamma - 1.0/c_{e2}}{1.0 - 1.0/c_{e2}}\right)^2\right\}, 1.0\right], \tag{2.38}$$

with the following constants to define the boundary layer and non-wake regions

$$\theta_{BL} = \frac{\overline{Re_{\theta t}}\mu}{\rho|u|} \quad , \quad \delta_{BL} = \frac{15\theta_{BL}}{2} \tag{2.39}$$

$$\delta = \frac{50\Omega d}{|u|}\delta_{BL} \quad , \quad Re_\omega = \frac{\rho\omega d^2}{\mu} \quad , \quad F_{wake} = e^{-\left(\frac{Re_\omega}{10^5}\right)^2} . \tag{2.40}$$

An empirical correlation, similar to Abu-Ghannam and Shaw, is formulated to relate the predicted transitional Reynolds number as a function of the turbulence intensity. Various correlations including the one used in the $\gamma - \overline{Re_{\theta t}}$ transition model are shown in figure 2–1. As the turbulence intensity increases, the transition Reynolds number is less sensitive to the turbulence intensity because the dominant transitional mechanism is bypass.

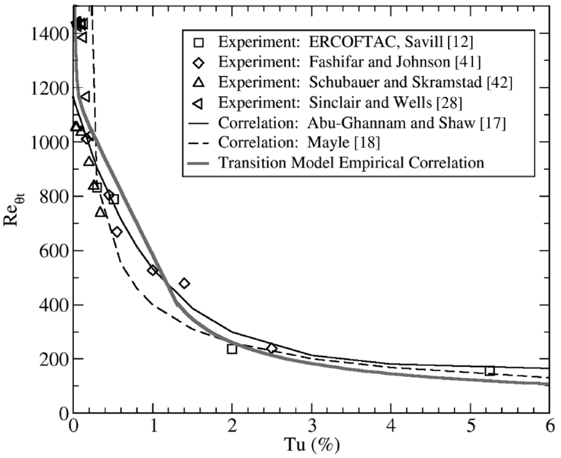

Figure 2–1: Langtry et al.'s flat plate correlations between $Re_{\theta t}$ and freestream turbulence intensity used in the $\gamma - \overline{Re_{\theta t}}$ transition model [13].

Equations (2.41), (2.42) and (2.43) are introduced to create this correlation. As equations (2.41), (2.42) and (2.43) can not be analytically solved, a shooting point iteration approach is used with an initial guess of $\lambda = 0$ and is updated ten times, which is where the differences between iterations becomes negligible.

The transition Reynolds number is equal to

$$Re_{\theta t} = \begin{cases} \left[1173.51 - 589.428Tu + \frac{0.2196}{Tu^2}\right] F(\lambda_\theta), & Tu \leq 1.3 \\ 331.50[Tu - 0.5658]^{-0.671} F(\lambda_\theta), & Tu > 1.3 \end{cases} \tag{2.41}$$

with the following correlation for equation (2.41)

$$F(\lambda_\theta) = \begin{cases} 1 - [-12.986\lambda_\theta - 123.66\lambda_\theta^2 - 405.689\lambda_\theta^3]e^{-\left(\frac{Tu}{1.5}\right)^{1.5}}, & \lambda_\theta \leq 0 \\ 1 + 0.275[1 - e^{-35.0\lambda_\theta}]e^{\left(\frac{-Tu}{0.5}\right)}, & \lambda_\theta > 0 \end{cases} \tag{2.42}$$

where θ is the momentum thickness,

$$\lambda_\theta = \frac{\rho\theta^2}{\mu}\frac{dU}{ds}, \tag{2.43}$$

Tu the freestream turbulence intensity,

$$Tu = 100\frac{\sqrt{2k/3}}{|u|} \tag{2.44}$$

and $\frac{dU}{ds}$ the acceleration in the streamwise direction. The following limits are imposed to improve the robustness of the transition model.

$$-0.1 \leq \lambda_\theta \leq 0.1, \quad Tu \geq 0.027, \quad Re_{\theta t} \geq 20. \tag{2.45}$$

To account for transition due to laminar separation of a boundary layer, an additional correlation must be made. The $\gamma - \overline{Re_{\theta t}}$ transition model simulates this by setting the intermittency to exceed 1.0 when the vorticity Reynolds number significantly exceeds the critical momentum thickness number. The intermittency from a separation bubble is

$$\gamma_{sep} = \min\left[s_1 \cdot \max\left\{0, \left(\frac{Re_v}{3.235 Re_{\theta c}}\right) - 1.0\right\} F_{reattach}, 2\right] F_{\theta t}, \tag{2.46}$$

where

$$F_{rettach} = e^{\left(\frac{R_T}{20}\right)^4} \quad , \quad s_1 = 2.0. \tag{2.47}$$

The effective intermittency that scales the turbulent production is defined as the maximum of either the intermittency or the separation intermittency.

$$\gamma_{eff} = \max(\gamma, \gamma_{sep}). \tag{2.48}$$

2.4.1 Farfield Transition Conditions

The transition model defines the farfield boundaries as [13]:

$$\gamma_\infty = 1.0 \quad , \quad \overline{Re_{\theta t}} = 1173.5 - 589.428 Tu_\infty + \frac{0.2196}{Tu_\infty^2}. \tag{2.49}$$

An inlet intermittency of 1.0 is chosen as to preserve the original turbulence model and turbulence decay rate. Using the zero pressure gradient relationships and the freestream turbulence intensity, equation (2.41) is employed so that $\overline{Re_{\theta t}}$ is set to the experimental correlations at the inlet.

2.4.2 Transition Wall Boundaries

A zero flux boundary condition is employed for both the intermittency and transitional onset Reynolds number [13]

$$\frac{\partial \gamma_{wall}}{\partial n} = 0 \quad , \quad \frac{\partial \overline{Re_{\theta t,\text{wall}}}}{\partial n} = 0. \tag{2.50}$$

2.5 $\gamma - \overline{Re_{\theta t}}$ Transition and $k - \omega$ SST Turbulent Model Modifications

To address challenges with the original $\gamma - \overline{Re_{\theta t}}$, the following changes are made for all simulations presented in this research.

- Eddy Viscosity: It was found through various simulations that at larger angles of attack, the transition model oscillated and over-predicted the coefficient of skin friction within the transition region [57]. A further restriction on the eddy viscosity as defined by Malan et al. [72] was employed,

  $$\mu_t = \rho k \ \min\left(\frac{1}{\omega}, \frac{a_1}{S\tilde{F}_2}, \frac{0.6}{\sqrt{3}S}\right),$$

  that resulted in smoother and more accurate coefficient of skin friction plots.

- Freestream Turbulence Boundary Conditions: The freestream turbulence variables k_∞ and ω_∞ are modified from the original definitions [73] to account for transition [72] and are defined as

  $$k_\infty = \frac{3}{2}(Tu_\infty U_\infty)^2, \quad \text{and} \quad \omega_\infty = \frac{\rho_\infty k_\infty}{R_\mu \mu_\infty}. \tag{2.51}$$

  with the ratio of viscosities being defined as

  $$R_\mu = \left(\frac{\mu_t}{\mu}\right)_\infty . \tag{2.52}$$

They are further modified to account for the non-physical turbulent dissipation [57, 74]

$$\omega_\infty = \left(\frac{\beta s}{U_\infty} + \frac{1}{\omega_\infty}\right)^{-1} \quad , \quad k_\infty = k_\infty \left(\frac{\beta \omega_\infty s}{U_\infty}\right)^{\frac{-\beta^*}{\beta}} ,$$

with s being the axial distance between the leading edge and inlet farfield and U_∞ the dimensionless freestream velocity. Note that for three-dimensional cases with swept wings, the distance that the flow travels before reaching the leading edge is different for each streamline. For the DLR-F5 testcase, s was defined as the minimum distance between the leading edge and the inlet farfield.

- F_{onset1}: Due to discrepancies of the transition region at higher angles of attack, most noticeable when greater than 5 degrees, and at high Reynolds numbers, an updated correlation to a parameter of equation (2.25) was made such that [57]

$$F_{onset1} = \frac{Re_v}{3.29 Re_{\theta c}}. \tag{2.53}$$

- Turbulent Wall Boundary: The specific dissipation energy (ω) wall boundary specified in the $k - \omega$ SST turbulence model by Menter et al. [69] was modified to account for the transitional model [72]

$$\omega_{\text{wall}} = \frac{6\nu}{\beta d^2}, \quad \text{where} \quad \beta = \beta_1 F_1 + \beta_2 (1 - F_1).$$

2.6 Implementation of $\gamma - \overline{Re_{\theta t}}$ Transition Model into the $k - \omega$ SST Turbulence Model

Once the two transition equations are solved, the effective intermittency is used in the $k - \omega$ SST turbulence model to scale the turbulent kinetic energy production and control transition as seen in the modified equations below (2.54).

$$\frac{D(\rho k)}{Dt} = \tilde{P}_\tau - \tilde{D}_k + \frac{\partial}{\partial x_j}\left[\left(\mu + \sigma_k \mu_t\right)\frac{\partial k}{\partial x_j}\right] + \tilde{A}_k, \tag{2.54}$$

$$\frac{D(\rho\omega)}{Dt} = \frac{\gamma}{\nu_t}P_\tau - \beta\rho\omega^2 + \frac{\partial}{\partial x_j}\left[\left(\mu + \sigma_\omega \mu_t\right)\frac{\partial \omega}{\partial x_j}\right] + 2(1-F_1)\frac{\rho\sigma_{\omega 2}}{\omega}\frac{\partial k}{\partial x_j}\frac{\partial \omega}{\partial x_j} + \beta\rho\omega_\infty^2, \tag{2.55}$$

where the production, destruction and ambient terms are scaled by the effective intermittency (γ_{eff}). The scaled production of turbulent kinetic energy is defined as

$$\tilde{P}_\tau = \gamma_{eff} P_\tau, \tag{2.56}$$

and a change is made from Menter's original production of equation (2.11) such that

$$P_k = \min(\mu_t S^2, 10 D_k), \tag{2.57}$$

with the following modifications to the destruction and ambient terms

$$\tilde{D}_k = \min(\max(\gamma_{eff}, 0.1), 1.0) D_k \qquad D_k = \beta^* \rho k \omega$$

$$\tilde{A}_k = \min(\max(\gamma_{eff}, 0.1), 1.0) A_k \qquad A_k = \beta^* \rho k_\infty \omega_\infty.$$

The modified destruction term ($\tilde{D}_k$) limits its scaling by the effective intermittency to between 0.1 and 1.0 to improve robustness. The ambient term ($\tilde{A}_k$) was introduced to counter-act the non-physical numerical dissipation in external testcases as a result of the destruction term. The same limits of effective intermittency are applied to the ambient term to balance the effect of the scaled destruction term.

Equation (2.14) has been modified due to the transition model such that:

$$R_y = \frac{\rho d \sqrt{k}}{\mu}, \quad F_3 = e^{-\left(\frac{R_y}{120}\right)^8}, \quad F_1 = \max(F_{1orig,F_3}). \tag{2.58}$$

Production of Intermittency

The intermittency production term (P_γ) of equation (2.24) is comprised of four parts: F_{Length} (equation 2.30) determines the length of transition, F_{onset} triggers the onset of transition (equation 2.25), $c_{a1}\rho S$ ensures the correct units/scaling and c_{e1} limits the maximum value of γ to 1.0 [57, 75]. A graphical representation of the important production terms γ, P_γ and F_{onset} are plotted on figures 2–2 and 2–3 with

$$y^+ = \frac{u^* d}{\nu}, \quad u^* = \sqrt{\frac{\tau_{wall}}{\rho}}. \tag{2.59}$$

The effect of these parameters on the turbulence variables k and μ_t are shown in figure 2–4.

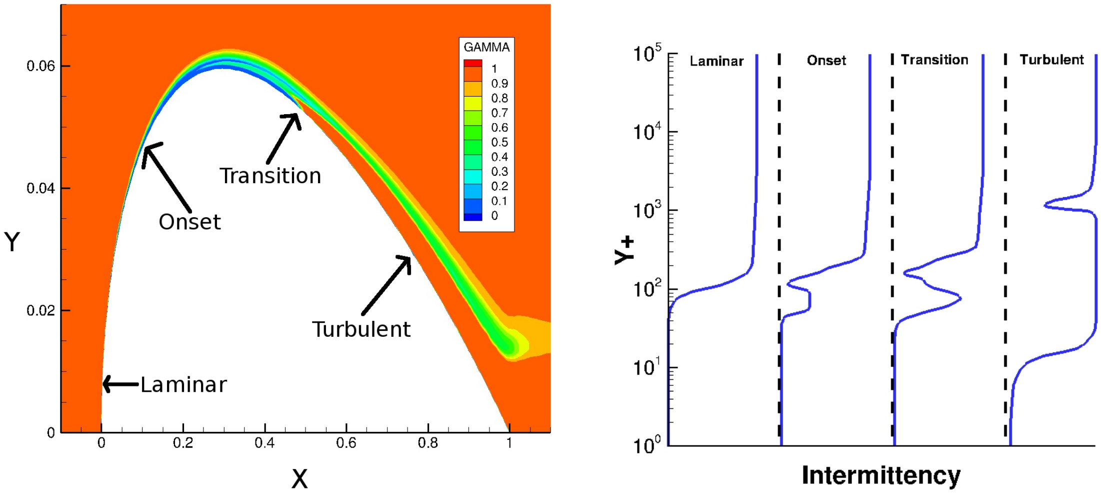

Figure 2–2: Intermittency over a NACA0012 airfoil.

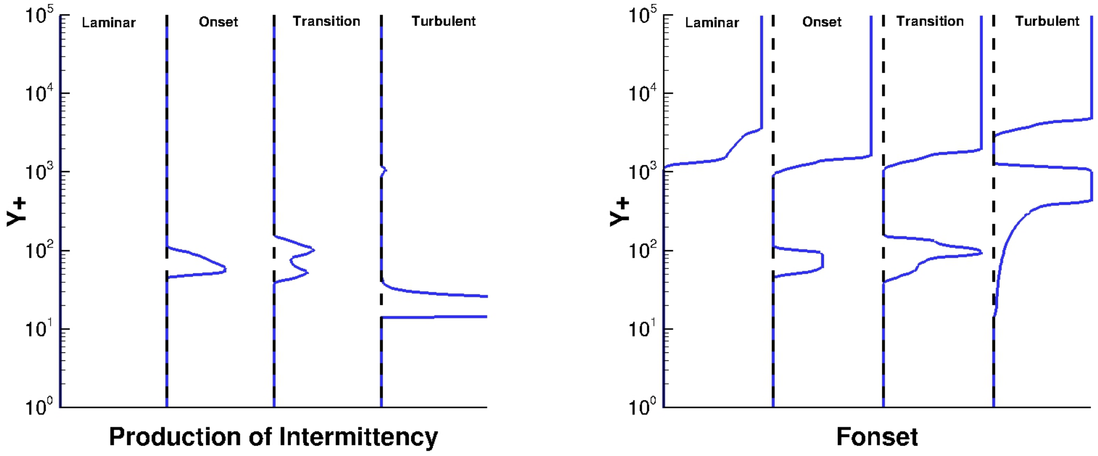

Figure 2–3: Production and Transition Onset Parameters over a NACA0012 airfoil.

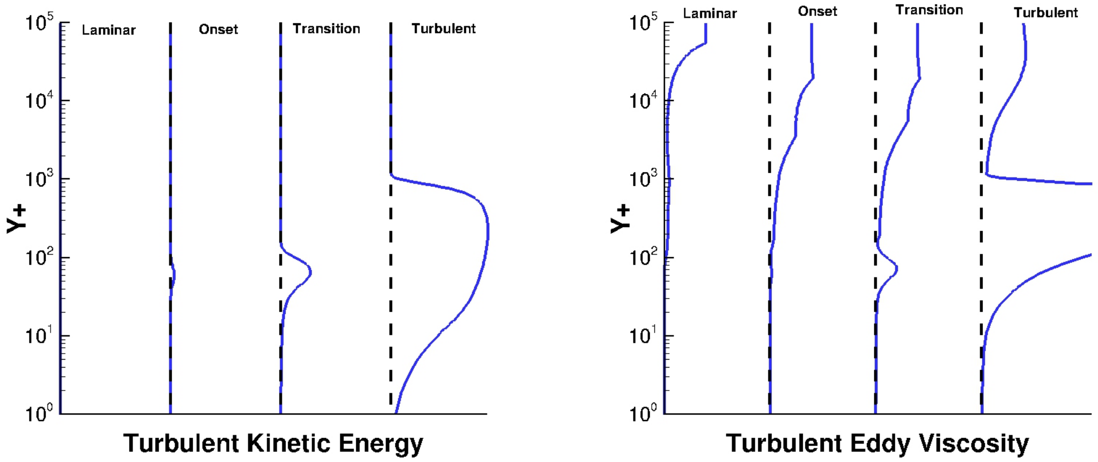

Figure 2–4: Turbulent Kinetic Energy and Turbulent Eddy Viscosity Parameters over a NACA0012 airfoil.

The γ, P_γ and F_{onset} profiles of a laminar, onset of transition, transition and turbulent section of the flow are plotted on the right-hand side of figure 2–2 and in figure 2–3. The approximate locations of these flow regimes are presented in the left-hand side of figure 2–2 .The y-axis corresponds to the non-dimensional distance from the wall. The contour plot of the intermittency across the upper surface of a NACA0012 airfoil is shown on the left hand side of figure 2–2. The blue area represents the laminar boundary layer which rapidly transitions into turbulent flow at roughly 40% of the chord. This turbulent boundary layer continued to grow along the airfoil until it reached the trailing edge. At a certain distance along the airfoil, labelled Onset in figures 2–2, 2–3, and 2–4, the vorticity Reynolds number exceeds a number that is a function of the $\overline{Re_{\theta t}}$ in the boundary layer which causes F_{onset} to become non-zero, producing intermittency. The rapid switch of F_{onset} leads to a rapid increase of the production of intermittency and causes the short transition from laminar to turbulent flow.

A numeric non-unity intermittency region occurred in various testcases simulated for this research between the turbulent boundary layer and turbulent freestream boundary conditions. The contour plot demonstrating this area can be found in the left hand side of figure 2–2 and is shown as the kink in the intermittency profile of the turbulent section in the right hand side of figure 2–2. This area is present in the simulation as a consequence of the numerical solution of the transition model and is not observed experimentally. It occurs because the production and destruction of the intermittency are zero outside the boundary layer leaving only the advection and dispersive terms in the transition model active. The laminar region before transition convects and dissipates downstream and eventually exits the boundary layer. As the destruction terms are close to zero outside of the boundary layer, this leads to a numerical solution where a non-unity intermittency region exists [57, 75]. It does not affect the solution as it only reduces the production of turbulent kinetic energy which is already at an inconsequentially small number outside the boundary layer.

The turbulent kinetic energy production term (equation 2.57), which is proportional to the strain and turbulent kinetic energy, is scaled by the effective intermittency (equation 2.56) due to the inclusion of the $\gamma - \overline{Re_{\theta t}}$ transition model. The effective intermittency (γ_{eff}) for this testcase is equal to the intermittency as there is no laminar separation. As both the strain and turbulent eddy viscosity are much smaller outside the boundary layer then inside, the further reduction of the small turbulent kinetic energy production term in this region does not have a noticeable effect on the flow solution. As seen in figure 2–4 the small area of reduced non-physical intermittency does not affect either the turbulent kinetic energy or turbulent eddy viscosity profiles. The purposes of this section is to demonstrate how the intermittency affects the flow and provide comparison data for researchers that develop transition models.

The $\gamma - \overline{Re_{\theta t}}$ model predicted the maximum value of the production of turbulent kinetic energy in the turbulent boundary layer to occur at $y^+ \approx 10$. This is consistent with various experimental data on flat plates though additional investigation is required to verify the characteristics of turbulent kinetic energy production in laminar, onset and transitional flow regimes [76, 77, 78].

Sensitivity of the $\gamma - \overline{Re_{\theta t}}$ model

The primary effect the $\gamma - \overline{Re_{\theta t}}$ transition model has on the turbulence model is scaling the production of turbulent kinetic energy by γ_{eff}. In turbulent flow, where

$\gamma_{eff} \approx 1.0$, the scaled turbulent kinetic energy is the same as if there were no transition model. In laminar flow the $\gamma_{eff} \approx 0.0$ and both the transition/turbulence models do not affect the general solution as there is minimal production of turbulent kinetic energy. In transitional regions the two models are tightly coupled but these regions tend to be small compared to the characteristic dimension for the test-cases investigated during this research and do not significantly effect the overall flow solution.

One of the limitations of the $\gamma - \overline{Re_{\theta t}}$ transition model is its sensitivity to the input freestream turbulence intensity (equation 2.44). An example of this sensitivity occurred when simulating the NASA airfoil at an angle of attack of zero degrees. It was found that a small increase of freestream turbulence intensity by 0.01% could change the transition location by more than 0.01 chord lengths. As mentioned in section 2.3, Menter's $k{-}\omega$ SST turbulence model blends the $k{-}\omega$ and $k{-}\epsilon$ turbulence models to reduce the $k - \omega$ model's sensitivity to the input freestream turbulence parameters. The addition of the $\gamma{-}\overline{Re_{\theta t}}$ transition model to the $k{-}\omega$ SST turbulence model results in the transition location and the solution being a strong function of the inlet freestream turbulence intensity thereby making the solution significantly dependent on user input variables.

The transition model was more sensitive to the the minimum grid size in the boundary layer than the turbulence model. In general, a maximum $y^+ < 1$ was required to accurately resolve the transition location along the wall though a $y^+ < 3$ was needed to resolve the turbulence model [31, 69]. If the $y^+ > 1$, the $\gamma - \overline{Re_{\theta t}}$ was unable to resolve the transition location and the airfoil was consequentially either completely laminar or turbulent.

2.7 Numerical Methods and Implementation

The testcases presented in this research were simulated using a pre-existing non-dimensional RANS code that was modified by the author to include the appropriate version of the $k-\omega$ SST turbulence and $\gamma-\overline{Re_{\theta t}}$ transition model.

To reduce round-off errors inherent in fixed precision computers, the Navier-Stokes equations are non-dimensionalized such that all solved variables have the same order of magnitude. These equations are not possible to be solved analytically for the majority of non-trivial testcases. Instead the equations are discretized and the domain is divided into geometric elements. The discretized governing equations are iteratively solved at the discrete points and when converged, they approximate the physical flow solution. Many discretiziation strategies exist but for this research the fluid flow was solved with a structured cell-centered finite-volume framework. The finite volume method was used as it allows for an arbitrary grid and satisfies the conservation laws over each volume element. As only steady-state testcases were simulated and time-accurate solutions were not investigated, the governing equations only needed to be discretized in the spatial directions and various converging schemes were used to increase their rate of convergence. The code was spatially discretized using a second-order central-difference scheme for the convective and viscous fluxes. As the code was cell-centered, the flux gradients along the faces are interpolated from the relevant cell-centered values. The second-order central-difference discretization used for the convection and viscous fluxes are prone to odd-even coupling and large errors at discontinuities. These issues were mitigated and the numerical stability improved by implementing a blended first- and third-order artificial dissipation scheme called the JST dissipation scheme [79].

The flow was solved using an explicit modified 4th order Runge-Kutta algorithm. A W-cycle multigrid, local time-stepping and residual averaging were employed to accelerate the convergence; however the turbulence and transition models were only solved at the finest grid level. At low Mach numbers, a Weiss-Smith flow preconditioner [57, 75], as provided below, was used to aid in the speed of convergence. The Weiss-Smith preconditioner is defined as

$$P_s = \begin{pmatrix} \beta & 0 & 0 & 0 \\ 0 & 1 & 0 & 0 \\ 0 & 0 & 1 & 0 \\ 0 & 0 & 0 & 1 \end{pmatrix},$$

where $\beta = M^2$. This preconditioner was employed for the low Mach number testcases for the NACA0012 and NLF(1)-0416 airfoils but was not used on the higher Mach cases for the DLR-F5.

The turbulence and transition equations are solved using a backwards-implicit Euler scheme. The advection terms in the turbulence and transition models were discretized using a first-order upwind scheme while the dissipation terms were discretized with a second-order central scheme. The resulting pentadiagonal matrix was solved implicitly in three dimensions using the Alternating Direction Implicit

(ADI) scheme [80]. The ADI scheme separates the pentadiagonal matrix into three tridiagonal matrices that were directly solved using the Thomas algorithm [81].

The simulated testcases used structured multiblock grids that were divided into smaller topologies to create a parallized environment. The computational standard of Message Passing Interface (MPI) created the framework for exchanging information between various computational resources running smaller topologies to create a cohesive solution.

Additional references for implementation and rationale can be found by Khayatzadeh et al. [56, 57, 58].

CHAPTER 3
Numerical Results

The numerical results of various testcases using the $\gamma - \overline{Re_{\theta t}}$ transition model will be presented and compared with experimental and computational data. No benchmark testcases were simulated by the author but several favourable flat plate results have been presented by Menter et al. [13, 31]. Three different geometries were simulated to examine the accuracy, robustness and versatility of the model in three-dimensional applications. The NACA0012 and NLF(1)-0416 airfoils were extruded along the spanwise direction to create quasi three-dimensional grids and were simulated at various angles of attack to verify against two-dimensional data. The third testcase simulated was the DLR-F5, a finite span wing-root setup, demonstrating the $\gamma - \overline{Re_{\theta t}}$ transition model's applicability in real-world applications.

3.1 Quasi Three-Dimensional NACA0012

The NACA0012 is a symmetric, non-cambered airfoil that was extruded in the spanwise direction to generate a quasi three-dimensional grid to validate the $\gamma - \overline{Re_{\theta t}}$ model. Some of the NACA0012 airfoil's applications include use in the horizontal tail of the Cessna 177 Cardinal [82] and the Cessna 172 wingtip [83]. It is a well studied airfoil with significant experimental data, presenting itself as a good non-trivial benchmark case for the transition model [1, 2]. The simulation was set up to correspond with the experimental parameters with the Reynolds number equalling 3×10^6 and the Mach number at 0.1 (incompressible regime). No experimental data was recorded for the turbulence intensity so it was set such that at an angle of 0.0 degrees the total drag was equal to experimental values; this corresponded to a turbulence intensity of 0.15%. A ratio of viscosities $\left(\frac{\mu_t}{\mu}\right)$ was not described in the experimental set-up but 10 was chosen as Menter et al. used the same value for similar problems [31].

A complete study of the RANS-turbulence-transition system of equations will be presented at a constant angle of attack of 1.0 degree. Next, the results for angles of attack from 0.0 to 12.0 degrees will be explored to examine the accuracy of the model over various flight conditions. Due to symmetry of the NACA0012, negative angles of attack have the same characteristics as their respective positive angle of attack. All simulations at various angles of attack for the NACA0012 converged to constant coefficients of lift, drag, skin friction and pressure drag though simulations occurred where the residual of all respective variables did not converge to machine zero in a reasonable simulation time.

3.1.1 Geometry and Grid

A structured C-H NACA0012 grid with 512 elements in the streamwise-direction, 256 in the direction of the surface normal and 16 along the spanwise direction is shown in figure 3–1.

Two symmetric boundaries were imposed on either end of the span. The farfield was 15 chord lengths away from the surface. A circulation correction was imposed at the farfield boundary. The grid was created with a maximum y^+ of 0.2, which is between the ranges of 0.001 and 1.0 recommended by Langtry. From simulations on flat plates, Langtry noted that grids with a $y^+ > 1.0$ predicted the transition location

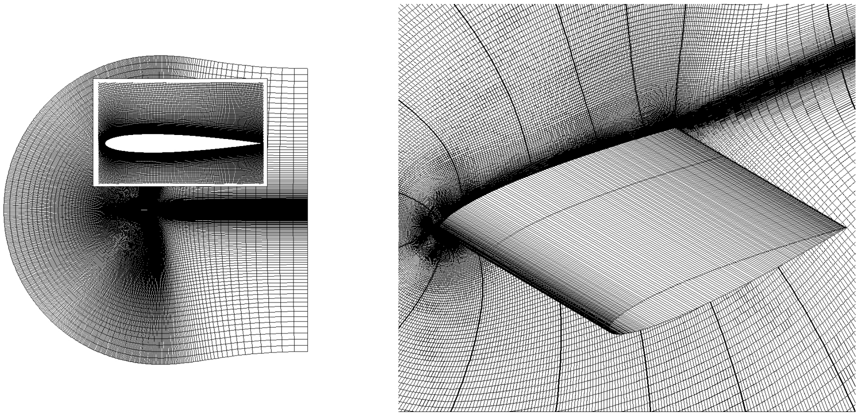

Figure 3–1: Grid of the 512x256x16 NACA0012.

too far upstream while grids with a $y^+ < 0.001$ the transition location tended to be too far downstream [31].

3.1.2 Convergence

The NACA0012 testcase at an angle of attack of 1.0 degree and Reynolds number of 3.0×10^6 was chosen to display the convergence of the flow, turbulence and transition residuals. The reduction of 12 orders of magnitude for the flow, turbulent and transition maximum residuals at an angle of attack of 1.0 degree is plotted in figure 3–2. The increases or spikes in the residual found in figure 3–2 occur due to the changes in the transition location. These spikes occur in the fluid flow within the transition region until the transition location is properly located.

Contour plots of variables of the transition model, primarily the intermittency, and the $\overline{Re_{\theta t}}$, are shown in figures 3–3, 3–4 and 3–5. As expected, due to the symmetry in the problem and the farfield boundary conditions, there exists zero crossflow. Therefore, $\frac{d\gamma}{dz} = 0$ and $\frac{d\overline{Re_{\theta t}}}{dz} = 0$ in the spanwise direction as shown in figure 3–3.

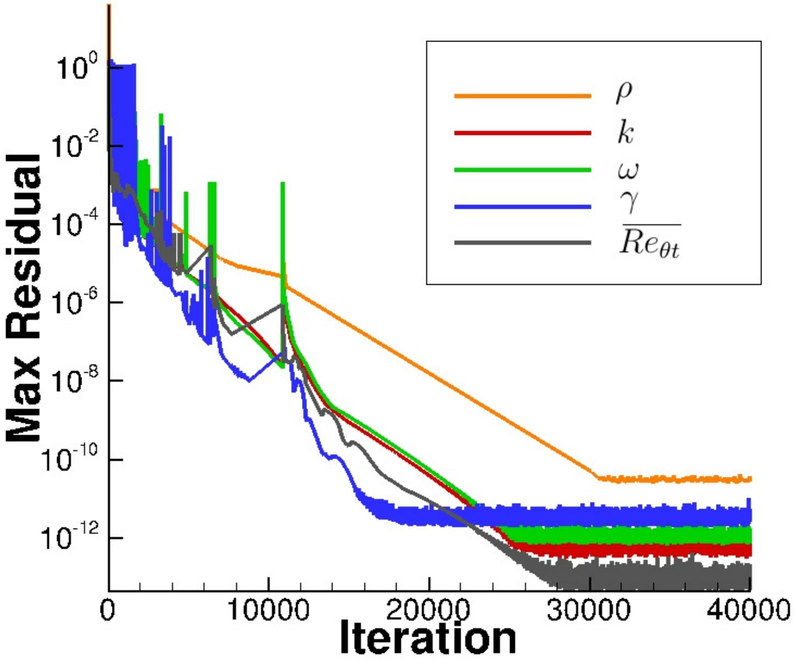

Figure 3–2: Maximum density, turbulent and transition residuals for the 512x256x16 NACA0012 at α=1 degree, M=0.1, Re=3.0×10^6, Tu=0.15%.

Figure 3–4 shows the contour plots of the intermittency and the $\overline{Re_{\theta t}}$ of a cross-section at midspan. In figure 3–4a, on the surface and in the laminar boundary layer the intermittency is low ($\gamma < 0.1$) compared with the completely turbulent ($\gamma = 1.0$) flow outside the boundary layer. The transition region can be seen in the zoomed-in region of figure 3–4a where a rapid shift from the blue/yellow/green laminar region to the red turbulence region occurs. The numerical non-unity intermittency region after transition is a result of the convection of intermittency in the model and not a physical phenomena. As detailed in section 2.6, this region does not effect the turbulent eddy viscosity.

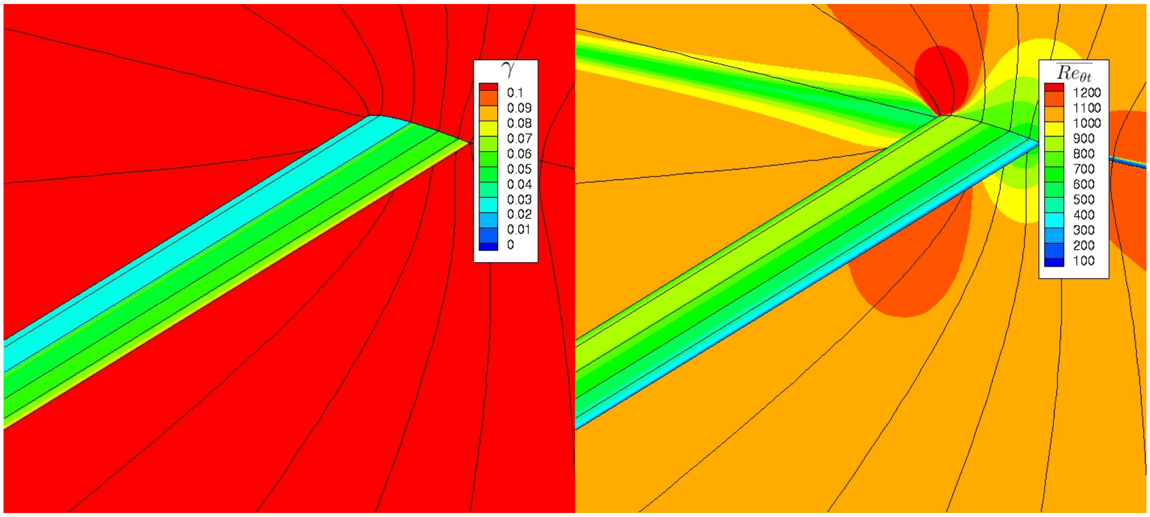

Figure 3–3: 512x256x16 surface and contour plot of the NACA0012 simulated at α=1.0, M=0.1, Re=3.0×10^6, Tu=0.15%. The intermittency or γ is presented on the left while the local transition onset momentum-thickness Reynolds number or $\overline{Re_{\theta t}}$ is on the right.

The $\overline{Re_{\theta t}}$ in figures 3–3 and 3–4b show how the presence of the favourable pressure gradient, starting from the leading edge to roughly 7% of the chord, increases the $\overline{Re_{\theta t}}$, which is the minimum Reynolds number needed for transition. The coefficient of pressure is shown in figure 3–6 demonstrating the switch from a favourable to adverse pressure gradient at 7% of the chord when the NACA0012 airfoil is at an angle of attack of 1.0 degree. After about 7% of the chord, the adverse pressure gradient reduces the $\overline{Re_{\theta t}}$ and the high $\overline{Re_{\theta t}}$ diffuses from the boundary layer into the freestream; this decreases the $\overline{Re_{\theta t}}$ and eventually leads to transition. A boundary layer for the $\overline{Re_{\theta t}}$ is seen in figure 3–4b though the $\overline{Re_{\theta t}}$ variable does not show significant deviations near transition as diffusion is the dominant mechanism.

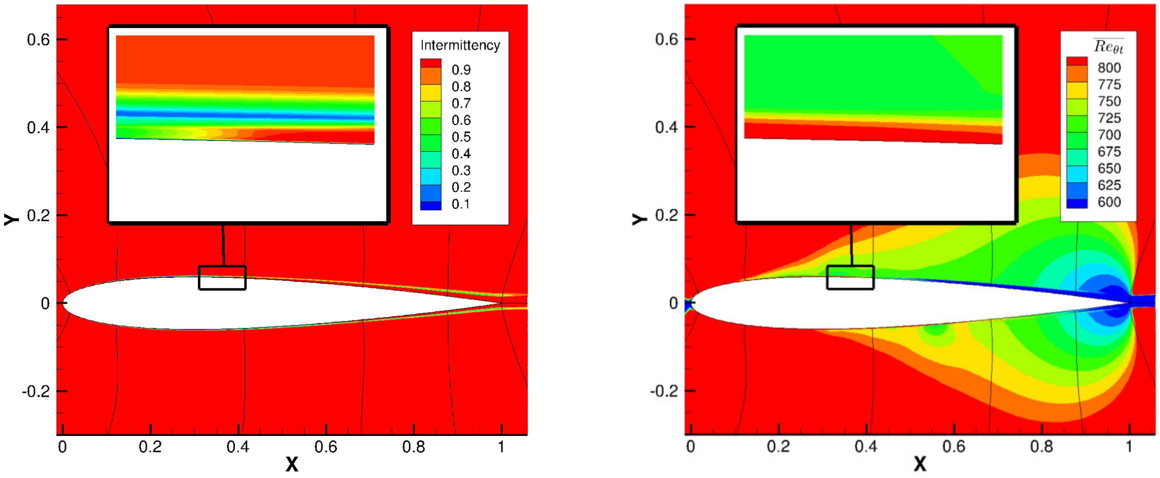

(a) Intermittency contours

(b) $\overline{Re_{\theta t}}$ contours

Figure 3–4: Transition variable contours of the NACA0012 512x256x16 at $\alpha = 1.0$.

Figure 3–5 shows the turbulent kinetic energy (k) and the specific rate of dissipation (ω) contour plots. The turbulent kinetic energy shows a rapid increase of k at the transition region and slowly grows until the trailing edge where it dissipates after the wake. The specific rate of dissipation (ω) in figure 3–5b demonstrates that ω decreases near the wall at transition, albeit gradually, due to the difference in laminar and turbulent flow.

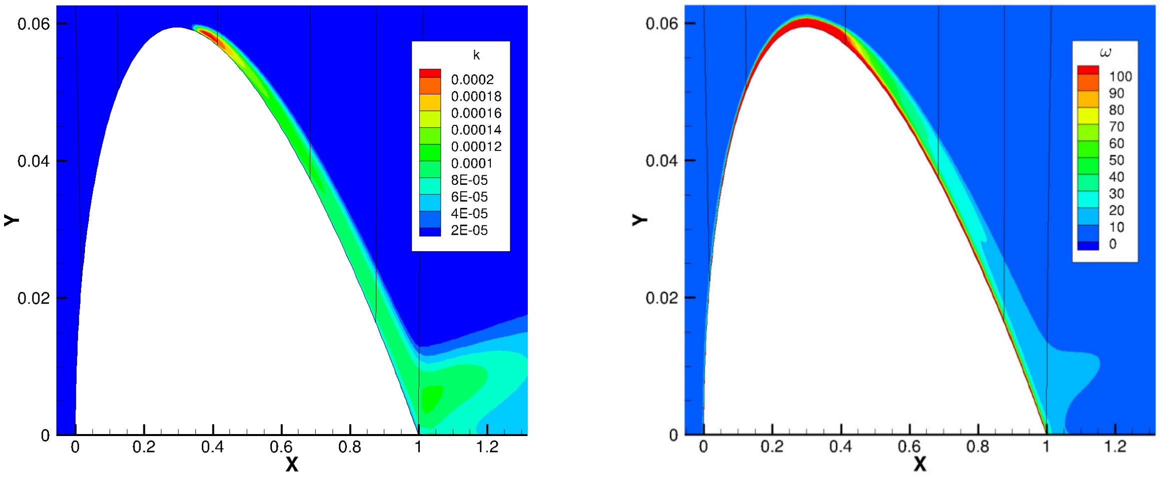

(a) k contours (Upper Surface)

(b) ω contours (Upper Surface)

Figure 3–5: Turbulence variable contours of the NACA0012 512x256x16 at $\alpha = 1.0$.

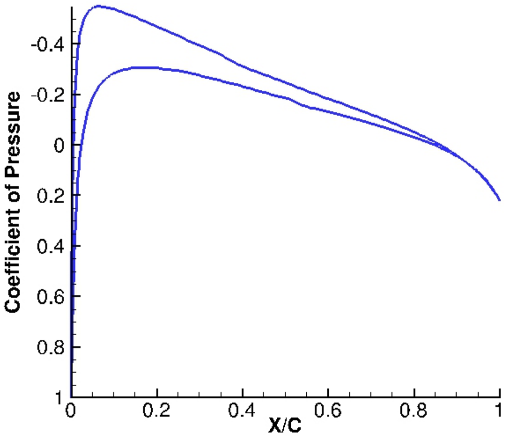

Figure 3–6: 512x256x16 coefficient of pressure along a NACA0012 airfoil at an angle of attack of 1.0 degree. A favourable pressure gradient is maintained for approximately 7% of the airfoil.

3.1.3 Comparison with Experimental and Computational Results

The results of the NACA0012 at a Reynolds number of 3×10^6 and Mach number of 0.1 will be compared against experimental data and additional simulation data [1, 2]. The coefficient of drag and coefficient of lift versus the angle of attack is shown in figure 3–7. Figure 3–7 includes the fully turbulent solution, which only uses the turbulence model, in order to show the effect the transition model has on the overall characteristics of the airfoil. The $\gamma - \overline{Re_{\theta t}}$ model compares favourably with the experimental data and shows strong correlations when the angle of attack is less than 8.0 degrees. At angles of attack higher than 8.0 degrees, a short laminar separation bubble is present near the leading edge for all simulations though experimental results intermittently show this phenomena [1]. An example of a short laminar separation bubble that appears in the simulation at $\alpha = 10.0$ on the upper surface is shown in figure 3–8a. Turbulent separation, demonstrated in figure 3–8b, also occurs at the same conditions mentioned. The NACA0012 tends to exhibit both leading-edge and trailing-edge type stall within the tested flight regimes making this airfoil particularly difficult to simulate and record consistent experimental/computational results at high angles of attack. The experimental discrepancies when the angle of attack is greater than 8.0 degrees may account for the decreased correlation of the transition model.

The experiment used to verify the transition model was conducted in 1970 and further research may have been performed to clarify the experimental data. At high angles of attack the transition point was either at the leading or trailing edge which were not useful points when validating the $\gamma - \overline{Re_{\theta t}}$ transition model. This reason, along with the time limitation, were why additional experimental data were not examined. Accurate experimental data regarding the size and location of the laminar separation bubble was not recorded and therefore could not be compared to the simulation results [1].

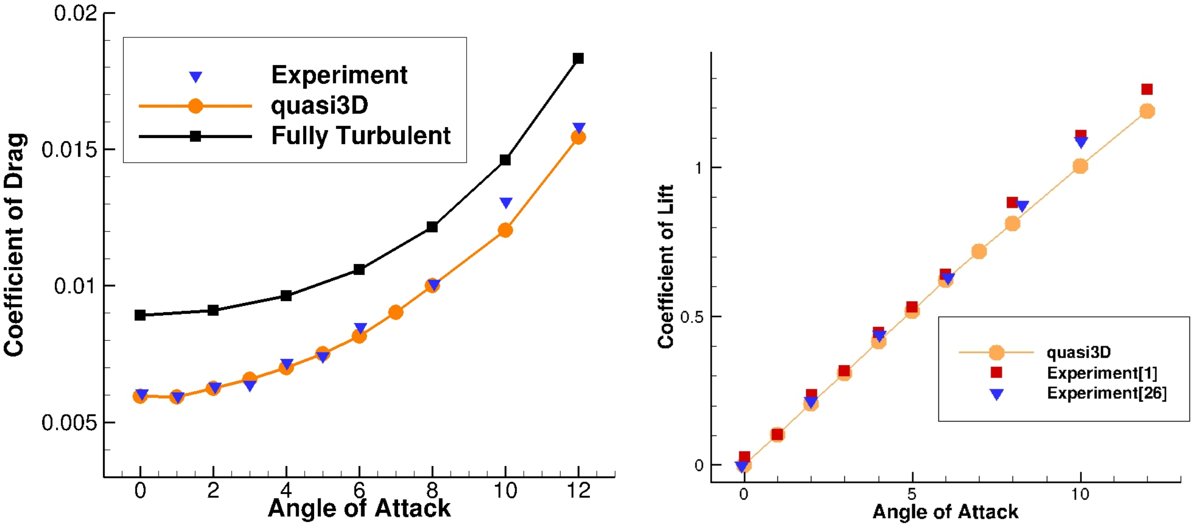

Figure 3–7: Coefficient of drag and lift versus angle of attack of the 512x256x16 NACA0012 at Re=3.0×10^6, M=0.1, Tu=0.15% [1, 14].

There is no formal definition of a transition point hence to make a fair comparison the start of transition of the transition model was matched to the definition of the start of the transition from the experiment. The experiment measured the onset of transition by the first onset of turbulence [1] from the China-Clay technique. The transition point for the $\gamma - \overline{Re_{\theta t}}$ was chosen such that transition occurs when turbulence levels increase from their minimum level along the surface which corresponds to an increase from the minimum intermittency set by the model at 0.02. As can be seen on figure 3–9 a rapid increase in skin friction and intermittency occurs just after 40% of chord. The increase of intermittency above its minimum value of 0.02

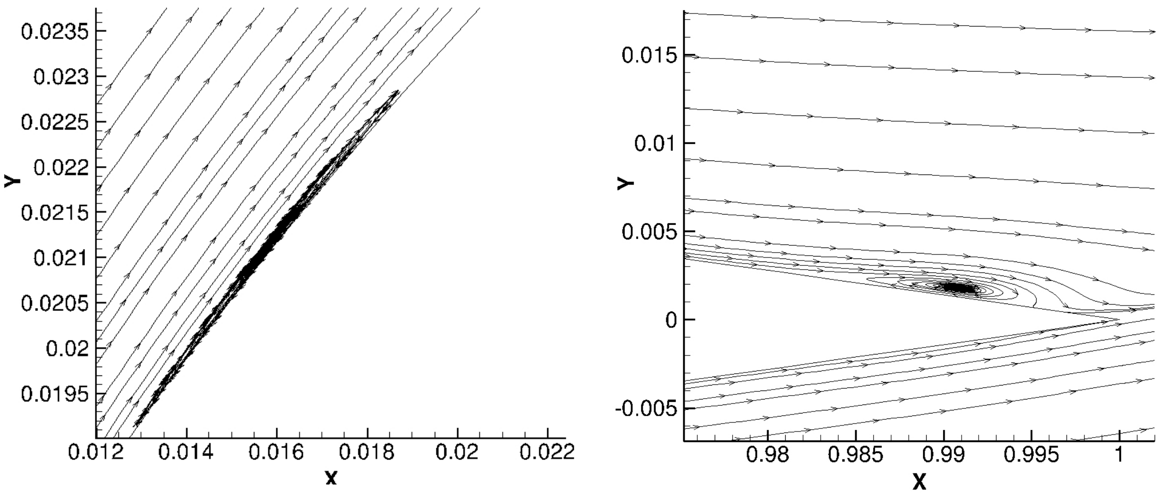

(a) Short laminar separation bubble near the leading edge

(b) Turbulent separation near the trailing edge

Figure 3–8: NACA0012 512x256x16 streamlines showing separation bubbles occurring on the upper surface at an angle of attack of 10.0 degrees.

occurs at 46% along the chord, which is near the half-way point of the increase of skin friction, and will be taken as the transition point.

The transition point versus the angle of attack is shown in figure 3–10 which shows strong agreement with experimental values. A comparison between the experimental and computational results of the transition locations for various angles of attack is shown in table 3–1. In addition to the $\gamma - \overline{Re_{\theta t}}$ model, two transition models implemented by Johansen [2] will be presented which include the e^n stability method and the one-step semi-empirical model of Michel [84]. The $\gamma - \overline{Re_{\theta t}}$ results compare well with the experimental data and predicts transition fairly accurately without having to know information *a priori* about the testcase.

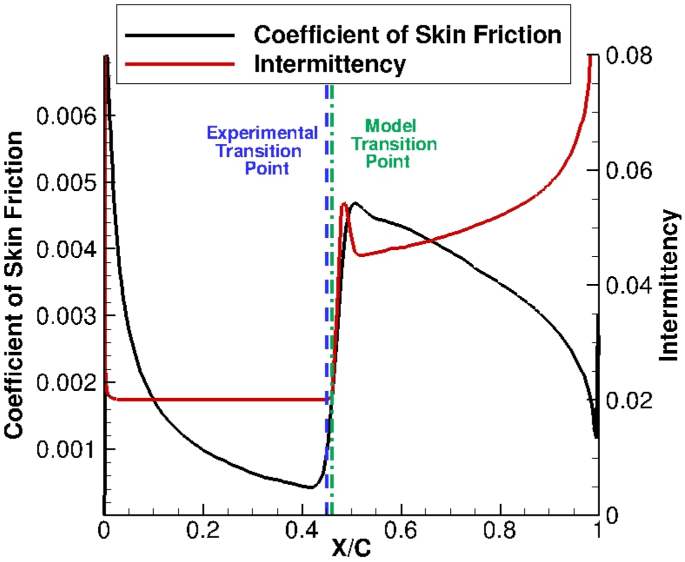

Figure 3–9: 512x256x16 NACA0012 cross-sectional skin friction and intermittency simulated at $\alpha = 0.0$, M=0.1, Re=3.0×10^6, Tu=0.15%.

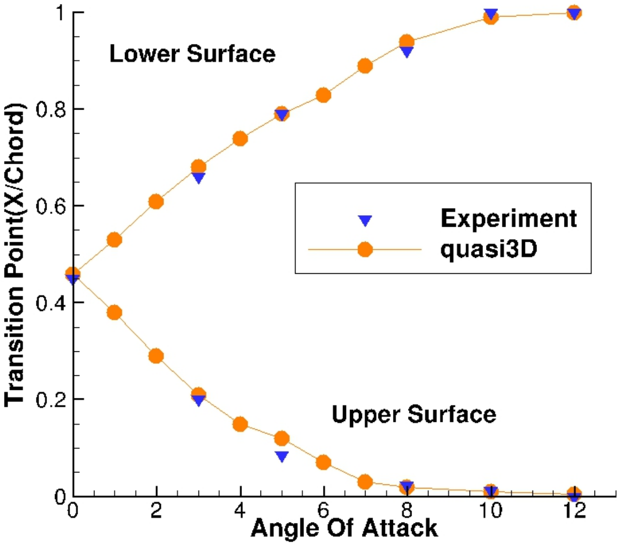

Figure 3–10: Transition point of the 512x256x16 NACA0012 at various angles of attack Re=3.0×10^6, M=0.1, Tu=0.15%.

	Upper Surface				Lower Surface			
α	Exp.	e^n	Michel	$\overline{Re_{\theta t}}$	Exp.	e^n	Michel	$\overline{Re_{\theta t}}$
0	0.45	0.44	0.43	0.46	0.45	0.44	0.43	0.46
3	0.20	0.19	0.21	0.21	0.66	0.68	0.72	0.68
5	0.085	0.06	0.13	0.12	0.79	0.84	0.88	0.79
8	0.024	0.025	0.070	0.010	0.92	0.99	1.00	0.94
10	0.013	0.014	0.040	0.010	1.00	1.00	1.00	1.00
12	-	0.012	0.014	0.005	1.00	1.00	1.00	1.00

Table 3–1: Transition point of the NACA0012 at various angles of attack compared with results from the experiments, Johansen's implementation of the e^n and Michel onset criterion and the $\gamma - \overline{Re_{\theta t}}$ transition model [1, 2].

For angles of attack up to 8.0 degrees, the $\gamma - \overline{Re_{\theta t}}$ transition model compares well with the experimental data and has an average error of the 1.0% chord length. At angles higher than 8.0 degree, the $\gamma - \overline{Re_{\theta t}}$ model still compares well but has noticeably worse errors on the upper surface compared to other transition models. The NACA0012 airfoil has maximum thickness at 12% of the chord which seems to indicate that the $\gamma - \overline{Re_{\theta t}}$ model's prediction of the transition region is less accurate within high curvature areas or in the presence of a strong pressure gradient. This is likely the result of the incorrect location of the laminar separation bubble. The transition model also predicts the transition point farther aft of the experimental values, making the $\gamma - \overline{Re_{\theta t}}$ model slightly conservative.

Figure 3–11 shows the coefficient of skin friction of the $\gamma - \overline{Re_{\theta t}}$ transition model compared against results by Johansen's e^n model. Both models have the same trend

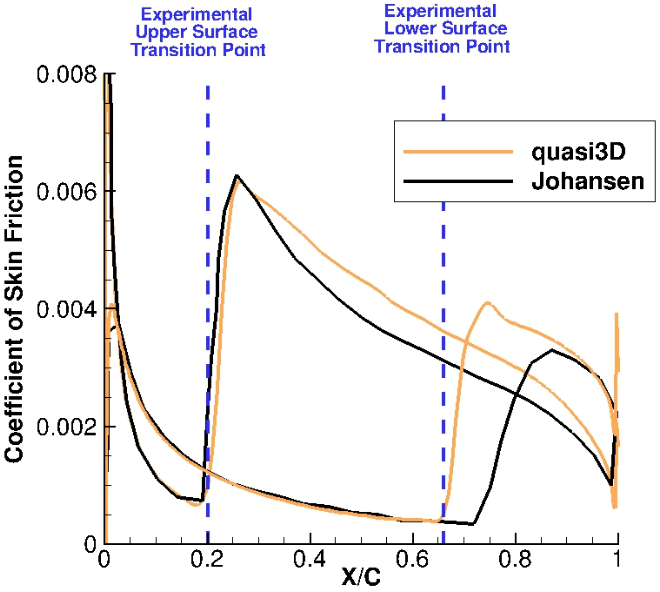

Figure 3–11: 512x256x16 NACA0012 skin friction comparison simulated at α=3.0, M=0.1, Re=3.0 × 10^6, Tu=0.15%.

for the laminar regime of the flow though deviations occurs within the transition and turbulent regions. The $\gamma - \overline{Re_{\theta t}}$ model predicts transition within 2% chord length of the experimental values while noticeable differences occur in the e^n model for the lower surface.

A profile of the coefficient of pressure is compared against experimental values [1] as seen in figure 3–12. A strong correlation with experimental values is found with little noticeable difference to the coefficient of pressure due to the transition.

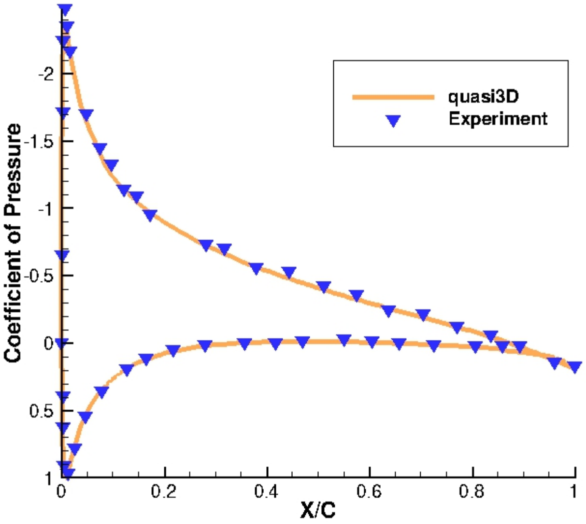

Figure 3–12: 512x256x16 NACA0012 coefficient of pressure simulated at α=3.0, M=0.1, Re=2.88 $\times$ 10^6, Tu=0.15% compared against experimental data.

3.2 Quasi Three-Dimensional NLF(1)-0416

The NLF(1)-0416 is a natural laminar airfoil that uses a favourable pressure gradient to achieve a relatively large region of laminar flow. Its use in low speed environments, large laminar region and depth of experimental data makes it an ideal airfoil to further verify the transition model. This airfoil was originally designed for general aviation purposes [15] but lately it has found use in wind turbine blades such as the Delft University of Technology's test turbine [85].

3.2.1 Geometry and Grid

The grid used was of C-H type where the NLF(1)-0416 two-dimensional airfoil was extruded resulting in the size of 512x256x16 or 2.1 million elements.

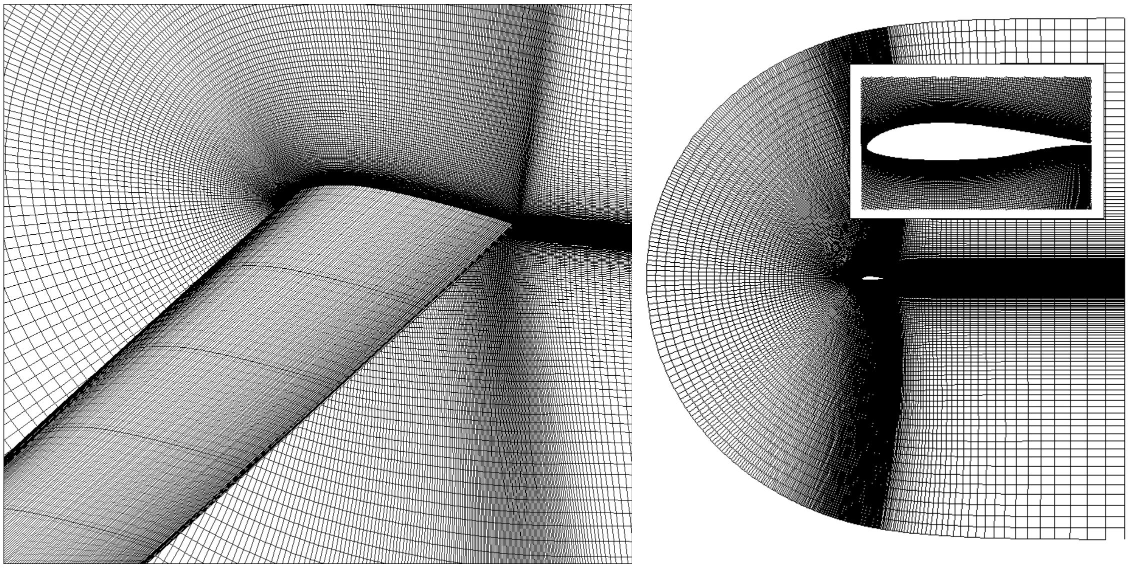

(a) Profile view with cross-section

(b) Cross-section at midspan

Figure 3–13: 512x256x16 NLF(1)-0416 three-dimensional grid.

The extrusion was constructed similar to the NACA0012 grid presented in section 3.1. A profile view and a cross-section at the midspan can be seen in figures 3–13a and 3–13b respectively. The farfield boundaries are approximately 10 chord lengths away and a circulation correction was used to improve accuracy. Symmetric boundary conditions were imposed on either end of the span to eliminate crossflow. The Reynolds number was set at 2.0×10^6, the Mach number at 0.1 and turbulence freestream intensity at 0.2% to match the experimental results. The maximum y^+ was equal to 0.1, much less than the 1.0 recommended by Langtry. A mesh study of the two-dimensional case which found a good compromise between mesh fineness and size can be found by Khayatzadeh [57].

3.2.2 Convergence

The convergence of the NLF(1)-0416 at an angle of attack of zero degrees will be shown in figure 3–14. Figure 3–14a shows the partial convergence of the flow, turbulent and transition variables. The transitional parameters reduce by three orders of magnitude and then oscillates since the transition point has not been fully resolved. The sudden drop in the maximum turbulent kinetic energy residual is from the freezing of the transitional parameters after 3,000 iterations. The lack of convergence of the flow and turbulence models after 3,000 iterations demonstrates that the transition model modifies the flow such that convergence is not possible for this configuration. It is conjectured that the numerical stiffness due to the inclusion of both a turbulence and transition model prevents the explicit RK time-stepping scheme from converging. It is thus recommended that an implicit scheme is employed as part of future work. Though the simulation did not locally convergence, the global variables of coefficient of lift and drag converged as seen in figure 3–14b. All NLF(1)-0416 testcases show this trend, though more iterations are needed to achieve convergence at higher angles of attack. A discussion on methods to improve convergence are discussed in section 4.2.1.

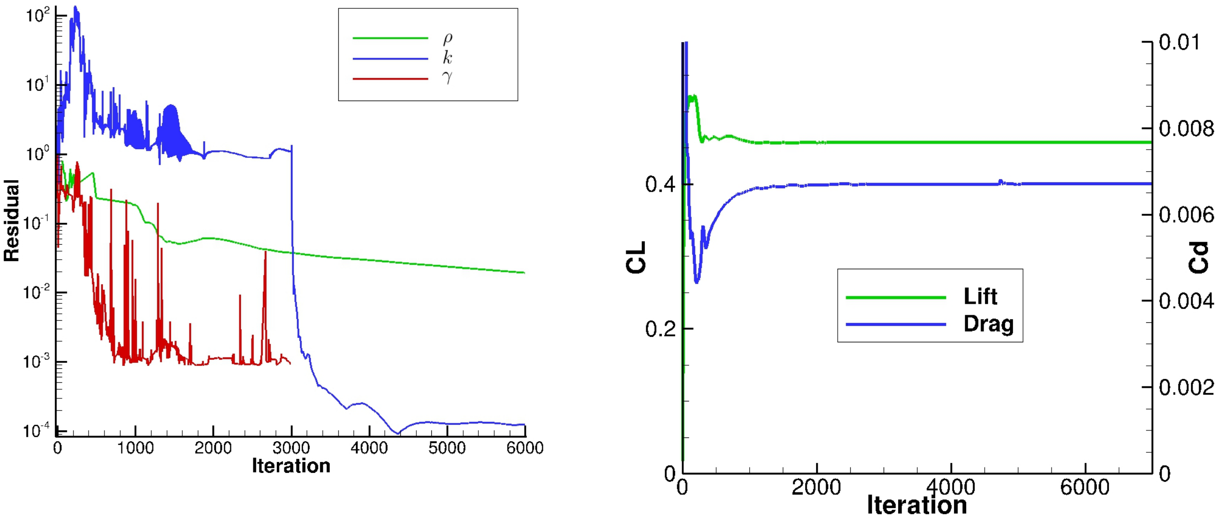

(a) Density, turbulent kinetic energy and intermittency maximum residual

(b) Convergence of the lift and drag

Figure 3–14: 512x256x16 NLF(1)-0416 convergence at M=0.1, α=0.0, Re=2.0×10^6, Tu=0.2%

Contours of the $\overline{Re_{\theta t}}$ are shown in figure 3–15a which again demonstrates that, as expected, no crossflow or variation in the spanwise direction occur. The intermittency values are seen in figure 3–15b which shows a more detailed area of transition. A non-physical non-unity intermittency region occurs after transition (shown in figure 3–15b) due to the formulation of the $\gamma - \overline{Re_{\theta t}}$ transition model as explained in section 2.6. The quick transition point is shown, similar to the NACA0012 transition point seen in figure 3–4a, though the NLF(1)-0416 has a transition point much farther downstream than the NACA0012.

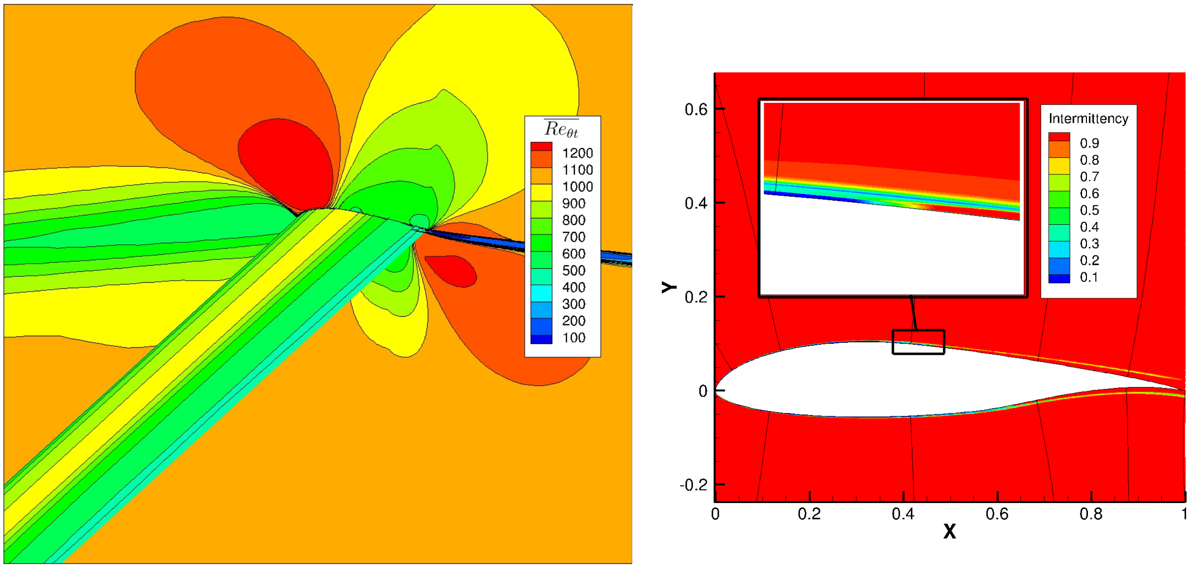

(a) $\overline{Re_{\theta t}}$ contour plot for the surface and symmetric boundary

(b) γ contour plots of a slice taken at midspan of the NLF(1)-0416

Figure 3–15: 512x256x16 transition variables of the NLF(1)-0416 at M=0.1, α=0.0, Re=2.0×10^6, Tu=0.2%.

3.2.3 Comparison with Experimental and Computational Results

The coefficient of pressure plot of the NLF(1)-0416 at an angle of attack of zero degrees is shown in figure 3–16. The three-dimensional transition model is compared against experimental values [15] and against the computation results of a two-dimensional code using the $\gamma - \overline{Re_{\theta t}}$ model [57]. As expected there is no noticeable difference between the two-dimensional and three-dimensional results though a small under-prediction of the coefficient of pressure for the transition model is seen.

A coefficient of skin friction plot is demonstrated in figure 3–17 which compares the current results against a two-dimensional code of the $\gamma - \overline{Re_{\theta t}}$ transition model [57] as well as computational results from the e^n model [86]. All results show the same laminar region and laminar separation bubble at transition but differ slightly on

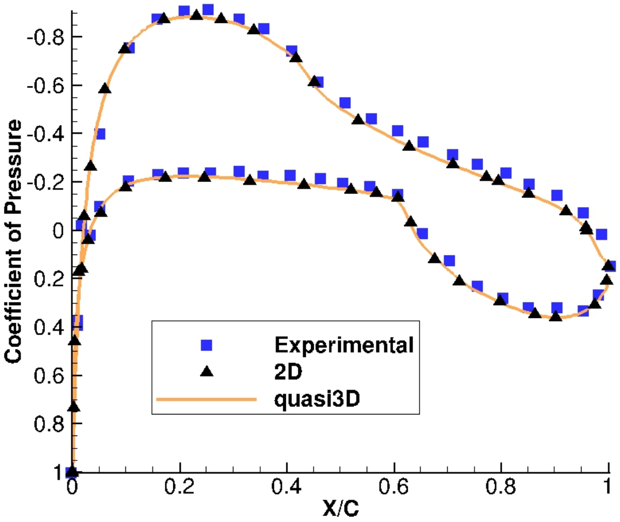

Figure 3–16: Coefficient of pressure of the 512x256x16 NLF(1)-0416 at M=0.1, Re=2.0×10^6, Tu=0.2% at α=0.0.

the transition location and turbulence region after. The laminar separation bubble is verified with experimental data for the upper and lower surface and show the transition model's ability to capture laminar-induced separation as well as the natural transition. The difference between the two-dimensional version by Khayatzadeh et al. [57] and the current research is likely caused by the lack of machine level convergence of the transition model.

As there exists little research into the convergence of the $\gamma-\overline{Re_{\theta t}}$ model and how strongly it is coupled to the turbulence model, it may be possible to have multiple locations for transition especially at unconverged solutions. One possible reason for the discrepancy is that the two-dimensional version of the code has the turbulence

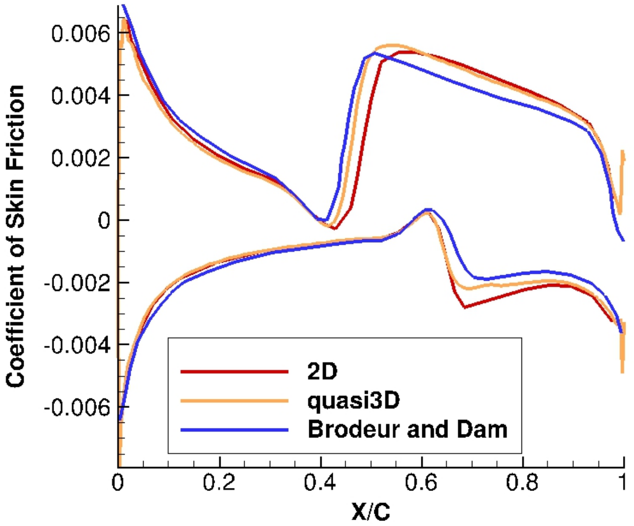

Figure 3–17: 512x256x16 skin friction of the NLF(1)-0416 at M=0.1, Re=2.0×10^6, Tu=0.2% and $\alpha = 0.0$

and transitional model coupled while this research uncoupled both equations. Further work and investigation is needed as no experimental data of the skin friction is known to the author.

The data comparing the experiment, two-dimensional and current research results are presented in table 3–2 at an angle of attack of one degree. There exists no noticeable difference between the coefficient of total drag, skin-friction drag, pressure drag or coefficient of lift between the two and three-dimensional versions. The experimental values match within the error of both versions of the code and demonstrate the ability of the $\gamma - \overline{Re_{\theta t}}$ transition model to capture the overall parameters of the airfoil *a priori*.

	C_L	C_D	C_{Dp}	C_{Df}
Current research	0.577	0.0069	0.0019	0.0050
2D Transition Model	0.577	0.0069	0.0019	0.0050
Experiment	0.570	0.0070	-	-

Table 3–2: Comparison of the NLF(1)-0416 at M=0.1, Re=2.0M and α=1.0 against experimental and computational data.

A range of angles of attack were simulated to compare the transition location and the drag polar of the NLF(1)-0416. The point of transition versus coefficient of lift was plotted in figure 3–18. In the experiment [15] turbulence was found acoustically using sensors along the airfoil so transition is only known to occur in a region defined by the open and closed shapes in figure 3–18. The transition model performs well at lower angles of attack or when $C_L \approx 0.5$ though deviations start to occur at higher angles of attack. In general the $\gamma - \overline{Re_{\theta t}}$ model predicts the transition point a bit far aft of the experimental values making it slightly conservative. Unlike the NACA0012 which almost shows a linear transition plot the NLF(1)-0416 shows less sensitive changes to the transition location around a C_L of between 0.3 and 0.5. This is expected as this airfoil is designed for cruise and minimum drag at a C_L of 0.4.

The drag polar of the NLF(1)-0416 is shown in figure 3–19 which compares the experimental values with the present study. The same trend of increased accuracy at lower angles of attack is seen.

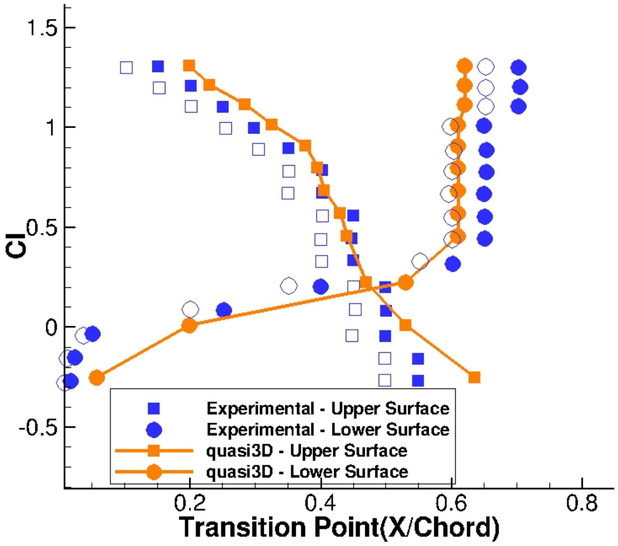

Figure 3–18: Transition point of the 512x256x16 NLF(1)-0416 at M=0.1,Re=2.0 × 10^6, Tu=0.2%. Open symbols correspond to a location where the flow is laminar; closed symbols, the flow is turbulent [15].

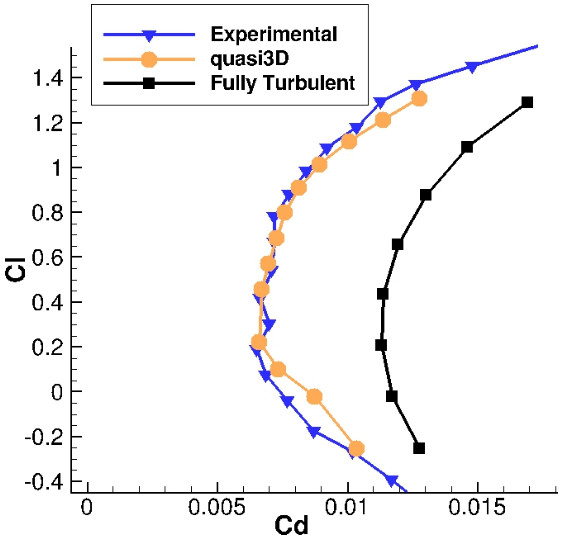

Figure 3–19: 512x256x16 NLF(1)-0416 drag polar at M=0.1, Re=2.0 × 10^6, Tu=0.2% [15].

3.3 DLR-F5

3.3.1 Geometry and Grid

The DLR-F5, a finite span three-dimensional wing, was simulated to validate the accuracy of the $\gamma - \overline{Re_{\theta t}}$ transition model on an industrial aviation testcase. The experiment was performed by Sobieczky where the transition location and pressure distribution was recorded over several spanwise locations over the finite wing [87]. The transition location was found using two methods: one used a sublimation technique while the other was extrapolated from the coefficient of pressure profiles.

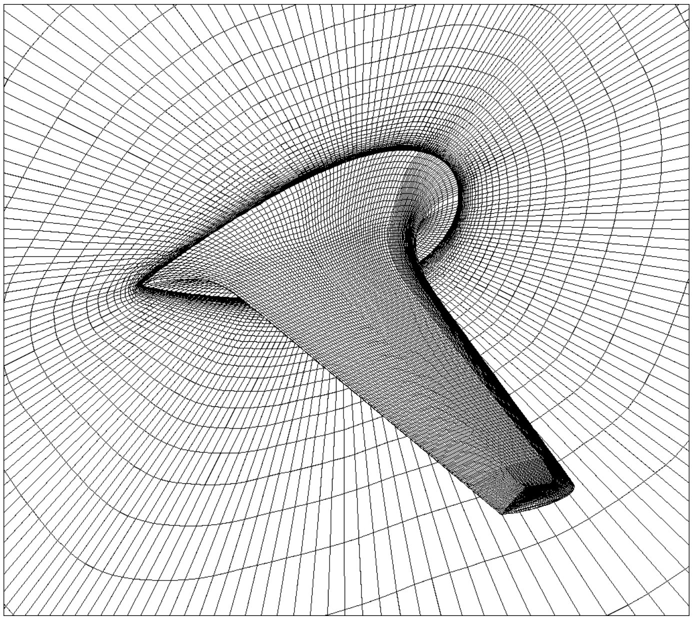

Figure 3–20: The surface and wall grid for the DLR-F5.

The DLR-F5 has symmetric airfoil sections, an aspect ratio of 9.5 and a 20 degree backward swept wing. The geometry being investigated has the wing root smoothly blended into the wall to eliminate horseshoe vortices. The simulation was transonic with a shock on the upper and lower surface when the Mach number was

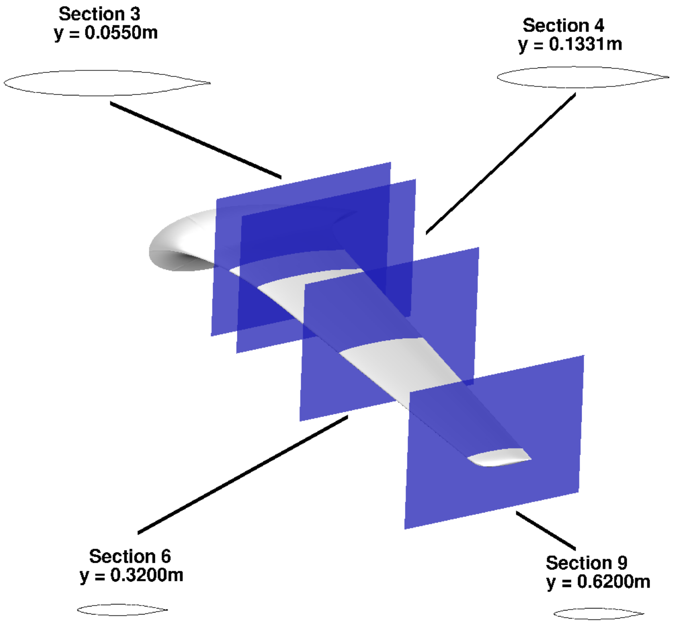

Figure 3–21: Two-dimensional profiles along various section of the DLR-F5

0.82, Reynolds number equalled 1.5×10^6 (based on the mean aerodynamic chord of 0.15m), freestream turbulence intensity was 0.5% and at an angle of attack of 2.0 degrees [87]. The mesh was generated based on the surface geometry of the DLR-F5 [88] and a 2 million grid point mesh was created using ICEM 15.0. A picture of the surface grid and wall section can be found in figure 3–20. The surface of the DLR-F5 is presented in 3–21 and various two-dimensional profiles along the span are shown.

3.3.2 Convergence

The global convergence of the lift and drag coefficients for this testcase are shown in figure 3–22.

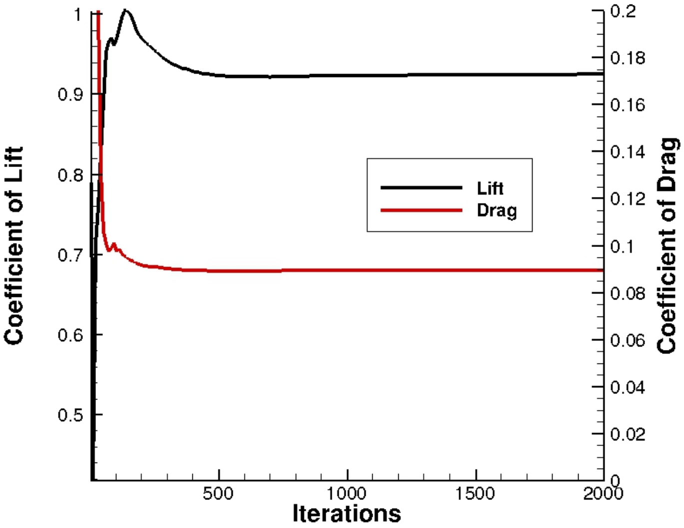

Figure 3–22: Global convergence of the DLR-F5 at M=0.82, α=2.0, Re=1.5 $\times$ 10^6, Tu=0.5%.

Though the simulation has reached a "steady-state", local maximum residuals are unable to reach machine precision. Some possible causes of the lack of local convergence is due to the large grid skew, lack of refineness near the shock/wake region and the grid spacing around the tip. The numerical stiffness introduced by both the transition and turbulence models as well as the computational grid could be alleviated with an implicit time stepping scheme and should be considered as part of future work. The grid used in the current research had 2.0 million elements compared to the 6.0 million elements used by Langtry [31] for the same testcase.

The y^+ value along the wing equalled 1.5 instead of the recommended value of 1.0 and was not further reduced as global convergence could not be reached at extremely fine boundary layer heights. A grid refinement study was not conducted due to time limitations.

3.3.3 Comparison with Experimental and Computational Results

Experimental results are compared against numerical results from this current research for the upper surface in figure 3–23 and the lower surface in figure 3–24. Note that the simulated transition occurs between the yellow and red contour regions. The $\gamma - \overline{Re_{\theta t}}$ transition regions for the upper and lower surfaces and are within the margin of error for both the experimental sublimination and pressure transition regions along the majority of the span. The zone between the dot-dashed grey lines in figure 3–23 shows the transition region found by Menter et al. and this research found transition almost halfway within this region.

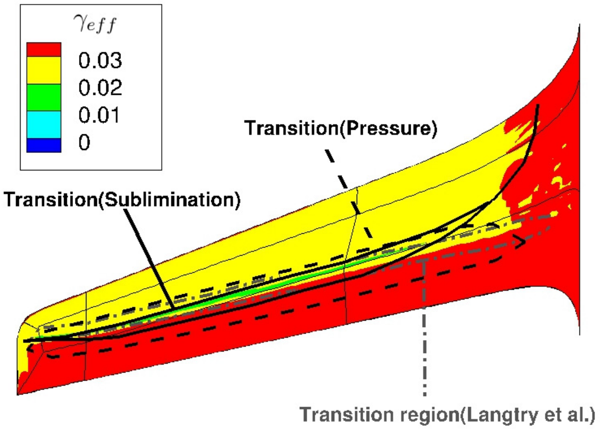

Figure 3–23: Transition location for the upper surface DLR-F5 at α=2.0.

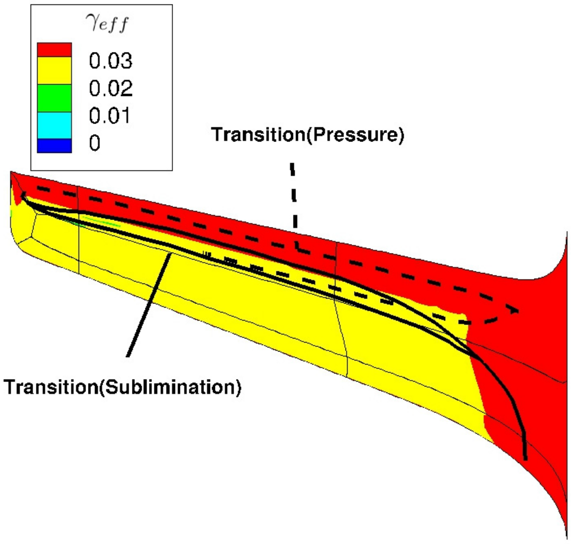

Figure 3–24: Transition location for the lower surface DLR-F5 at α=2.0.

The $\gamma - \overline{Re_{\theta t}}$ predicts two separate transition regions. The first is the result of a turbulent boundary layer of the wall/splitter plate growing and contaminating the wing root boundary layer prematurely turning it turbulent. This region in the current research is much larger than the same zone found by Langtry et al. [13] and can be compared in figure 3–31. This discrepancy is likely a result of the grid's coarse nature near the tunnel side wall where the boundary layer is not properly captured. The $y^+ > 25$ along the tunnel side wall may have resulted in a larger turbulent boundary layer which contaminated the boundary layer of the wing root. Grids with a smaller y^+ near the side wall were simulated though global convergence could not be reached. An additional difference in the models is the inclusion of an ambient term in the turbulent equations and the modification to the definition of the freestream turbulence intensities, seen in equation (2.53). This contaminated region shows poor correlation with experimental data because of the non-included crossflow instability corrections in the $\gamma - \overline{Re_{\theta t}}$ model.

The second transition regime is the shock induced laminar separation where the simulated transition location is within the regions described by the experimental pressure and sublimination techniques.

At halfway along the span where $y = 0.3200m$ the intermittency, $\overline{Re_{\theta t}}$, Mach number and eddy viscosity are shown in figures 3–25 and 3–26. After the shock, as seen in figure 3–26a, a small laminar separation bubble occurs that quickly transitions and reattaches as turbulent flow. Note the small laminar separation bubble can be seen in the recirculated flow in the zoomed-in portion of figure 3–26a. This transition can be seen with the large increase in intermittency in figure 3–25a or the increase in μ_t in figure 3–26b.

The same trends as above occur farther along the span at $y = 0.6200m$ are are shown in figures 3–27 and 3–28. This demonstrates the $\gamma - \overline{Re_{\theta t}}$ transition model's ability to capture shock induced separation.

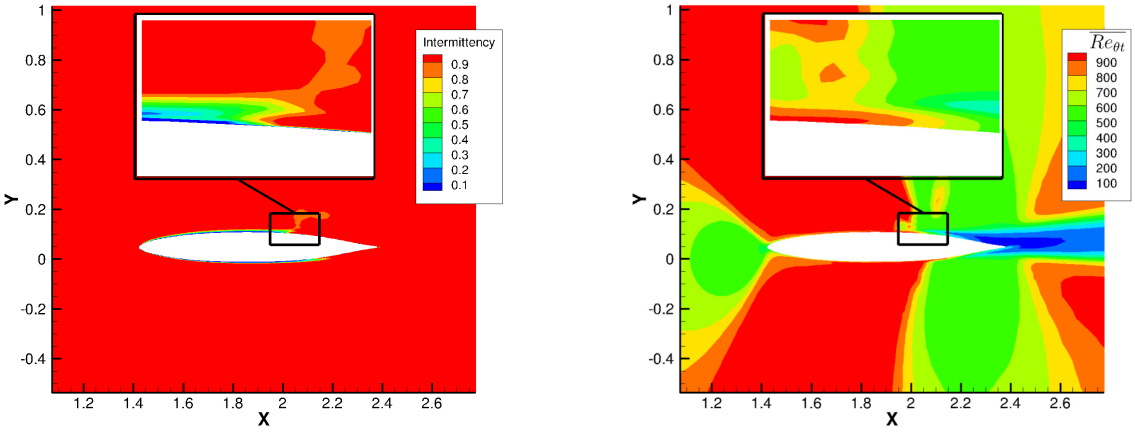

(a) γ contours (b) $\overline{Re_{\theta t}}$ contours

Figure 3–25: γ and $\overline{Re_{\theta t}}$ contours of the DLR-F5 at section 6 where $y = 0.3200$m, $\alpha = 2.0$, Re=1.5×10^6, M=0.82.

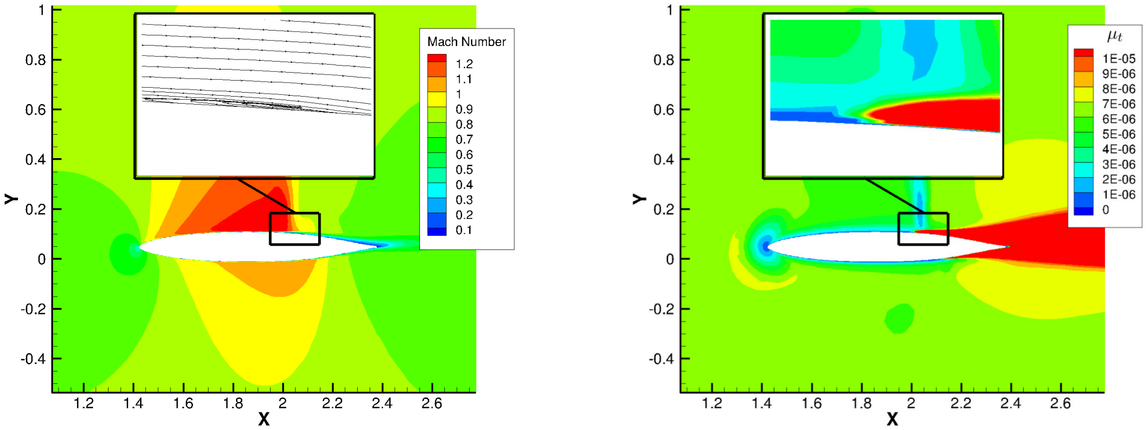

(a) Mach contours (b) Turbulent Eddy Viscosity (μ_t) contours

Figure 3–26: DLR-F5 contours at section 6 where $y = 0.3200$m, $\alpha = 2.0$, Re=1.5×10^6, M=0.82.

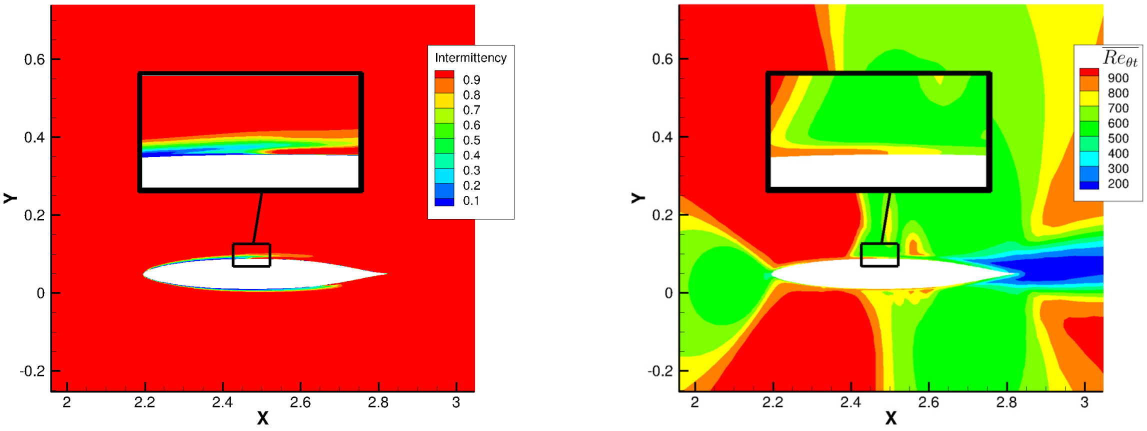

(a) γ contours (b) $\overline{Re_{\theta t}}$ contours

Figure 3–27: DLR-F5 γ and $\overline{Re_{\theta t}}$ contours at section 9 where $y = 0.6200$m, $\alpha = 2.0$, Re=1.5×10^6, M=0.82.

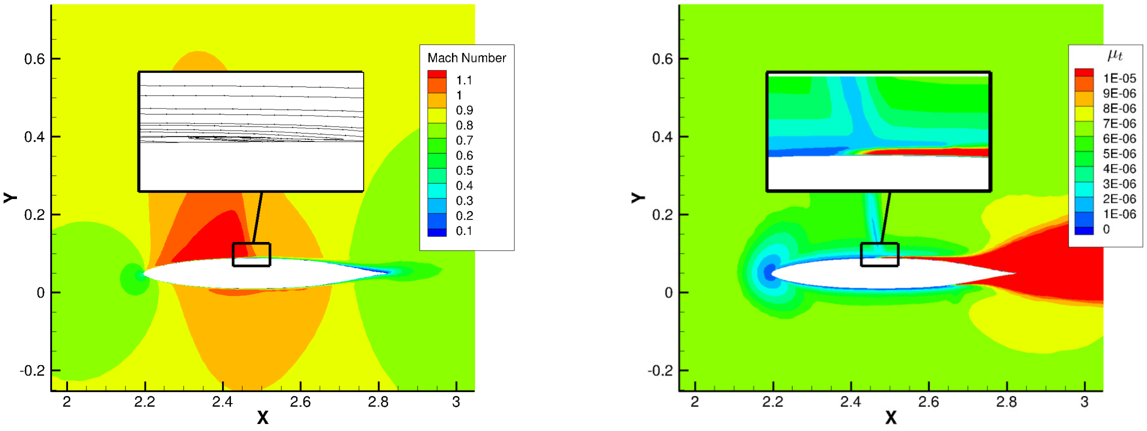

(a) Mach contours (b) Turbulent Eddy Viscosity (μ_t) contours

Figure 3–28: DLR-F5 contours at section 9 where $y = 0.6200$m, $\alpha = 2.0$, Re=1.5×10^6, M=0.82.

As the DLR-F5 has a 20 degree swept wing it is on the cusp where crossflow instabilities are the dominant transitional mechanism. As figure 1–10 demonstrates for a conceptual aircraft, a wing sweep of 20 degrees means a transition location due to crossflow instabilities occurs at less than 5% of the chord. The $\gamma - \overline{Re_{\theta t}}$ transition model lacks a crossflow correlation which is likely why the simulated transition region does not smoothly blend along the span but rather has two distinct sections. It is possible to append a term into the transitional model so a crossflow correlation can be added but none were found before the publication of this thesis.

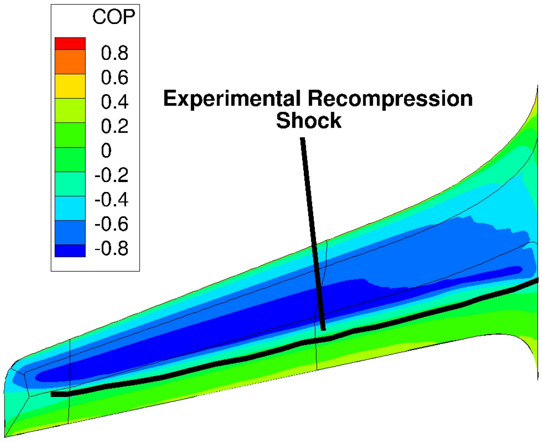

Figure 3–29: Shock location and pressure contours on the upper surface of the DLR-F5.

Figure 3–29 compares the location of the recompression shock on the upper surface with the transition model. The transition model predicts the shock slightly farther upstream of the experimental shock though the slight upstream movement of the shock along the span is seen. The coefficient of pressure plots, seen in figure 3–30, along four cross-sections of the DLR-F5 confirm that the transition model places the shock too far upstream. The transition model compares well in the laminar region and turbulent regions but deviates at transition.

The coefficient of skin friction and surface streamlines are plotted in figure 3–31 comparing the results of Langtry and Menter [13] and the current research. There are major visual discrepancies between different versions of the $\gamma - \overline{Re_{\theta t}}$ transition model that include the size of the shock induced laminar separation bubble, the size of the turbulent boundary layer near the wall, the streamline directions after the shock and the increase of skin friction near the tip. Though these discrepancies are likely a result of the modifications made to the transition model or grid, further investigation is needed to determine the exact causes.

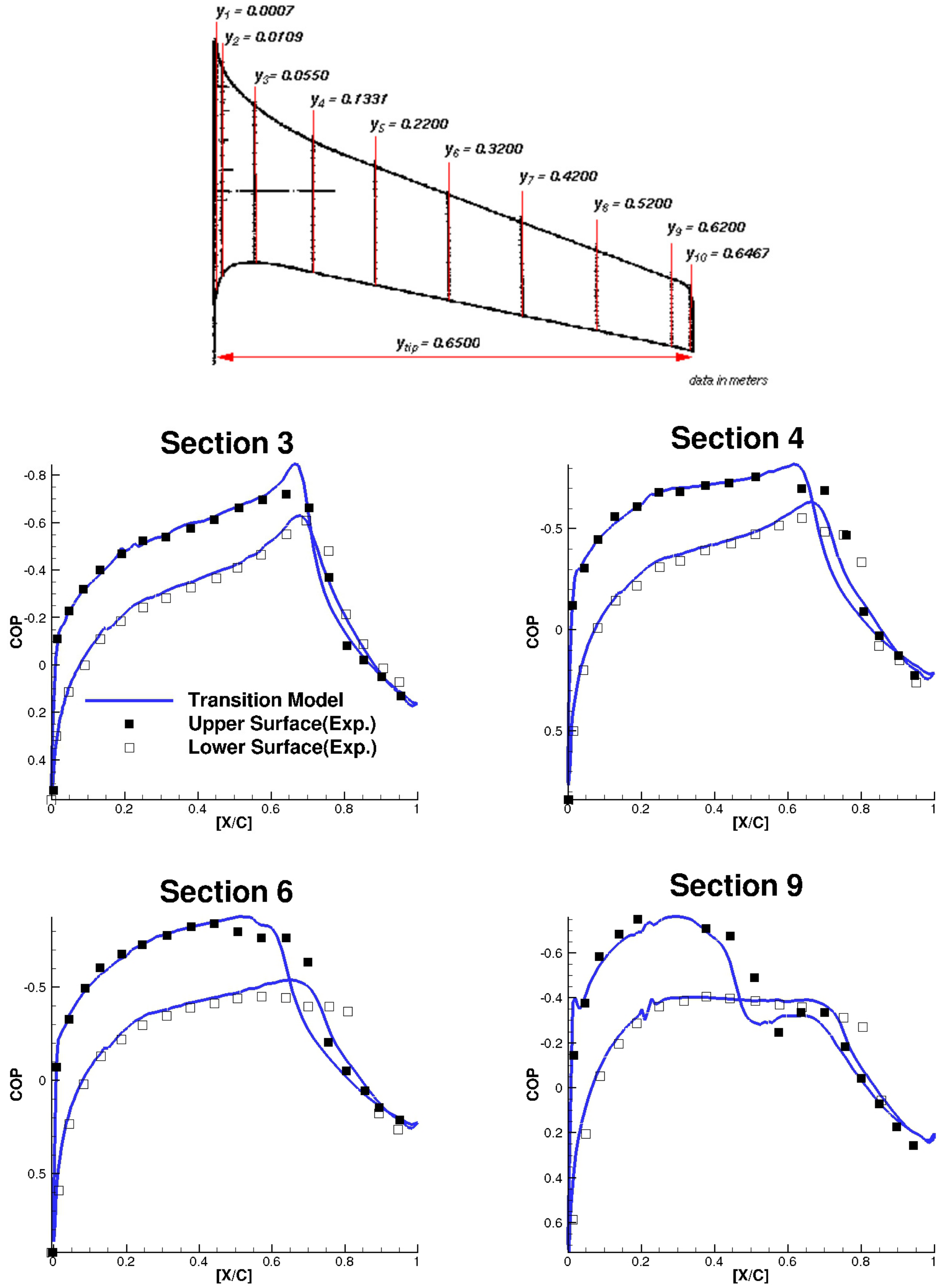

Figure 3–30: Coefficient of pressure along various cross-sections of the DLR-F5, α=2.0, Re=1.5×10^6, M=0.82

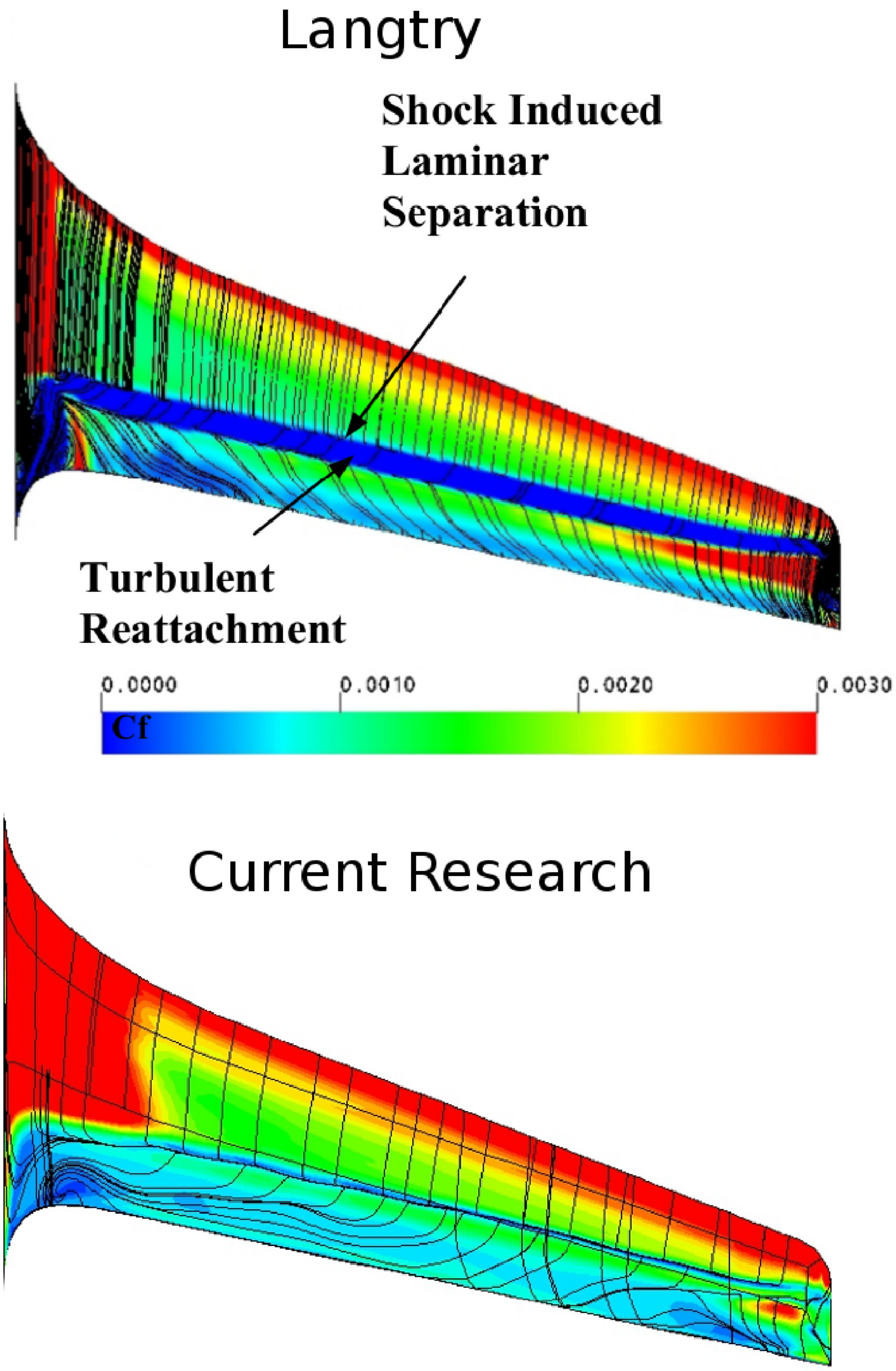

Figure 3–31: Coefficient of skin friction and streamline comparison of the DLR-F5 [13].

CHAPTER 4
Conclusions

4.1 Summary

Transition is an important phenomenon in aerodynamic applications though it is not implemented in most modern commercial CFD codes. The $\gamma - \overline{Re_{\theta t}}$ transition model holds promise to include first-order effects of transition and be compatible with unstructured, parallel execution with non-trivial geometry. As computational aircraft design and optimization becomes more prevalent, an accurate transition model will be critical for the next generation of aircraft.

The $\gamma - \overline{Re_{\theta t}}$ is a two equation transport model used in a Reynolds-averaged Navier-Stokes environment that solves for the intermittency and the local transition onset momentum-thickness Reynolds number. This approach models both the local and non-local effects such as adverse pressure gradients or high induced freestream turbulence intensity as well as predicts various transitional mechanisms such as natural, bypass, shock induced and separation induced transition. The $\gamma - \overline{Re_{\theta t}}$ was also able to model complex flow behaviour such as laminar and turbulent separation on the same testcase.

The $\gamma - \overline{Re_{\theta t}}$ transition model successfully predicted transition locations for various angles of attack for the NACA0012 and NLF(1)-0416 airfoils. In general, lower angles of attack were more accurate than higher angles of attack. The finite span wing DLR-F5 demonstrated the ability for the $\gamma - \overline{Re_{\theta t}}$ model to simulate industrial aviation geometries with various transitional mechanisms. The transition model compared well with the DLR-F5 experiments though deviations do occur near the wing-root as the model did not include correlations for transition due to crossfow instability. The $\gamma - \overline{Re_{\theta t}}$ holds promise to accurately predict the location of transition on complex geometry though additional research is required to improve the stability and convergence.

4.2 Transition Model Improvements

4.2.1 Convergence and Stability

There exists few studies on the convergence of the $\gamma - \overline{Re_{\theta t}}$ transition model leading to a lack of consensus on the optimum methodology to solve the turbulence/transition variables. The stability and accuracy of the model is also affected by the ω wall condition though this author has not seen an investigation of its impact. Not all cases in this research converged to machine zero and further work is needed to investigate this issue along with its solution. Mosahebi and Laurendeau [89] performed a two-dimensional convergence study which investigated various methods used to improve convergence for the $\gamma - \overline{Re_{\theta t}}$ model. One proposed method that led to convergence was to use a fully segregated underelaxed scheme between the turbulence and transition model such that

$$\gamma_{eff}^{new} = (1.0 - \alpha)\gamma_{eff}^{old} + \alpha\gamma_{eff},$$

where $\alpha = 0.1$. Though this correction was not implemented for this research, the results in Mosahebi and Laurendeau hold promise on improving convergence for three-dimensional applications.

4.2.2 Crossflow Correlations

The non-linear interaction between Tollmien–Schlichting, stationary and travelling crossflow disturbances create challenges to formulating crossflow transition models. Several correlations to include the crossflow instabilities into the $\gamma - \overline{Re_{\theta t}}$ transition model have been proposed with further work being done to refine and validate various models. Some examples include using the gradients in the crossflow direction by Grabe et al. [90] and using the local helicity ($H = |u_i \cdot \Omega_i|$) by Müller et al. to trigger the production of intermittency. There is no consensus on the best methodology and none yet show wide applicability on three-dimensional cases.

4.3 Future Work

To further validate, improve and extend the $\gamma - \overline{Re_{\theta t}}$ transition model the following items are suggested:

- determine a framework to study the stability of the model and investigate the reasons behind the lack of machine level convergence
- implement a crossflow instability correlation
- determine a robust method of determining freestream turbulent dissipation for arbitrary geometry
- simulate additional three-dimensional testcases, such as the CRM wing (with comparison of computational transition data by Coder et al. [91]), to determine if the modifications made to the model cause inaccuracies at high Mach numbers
- implement an optimization framework for a complete three-dimensional wing optimization

REFERENCES

[1] N. Gregory and C. O'Reily. Low-speed aerodynamic characteristics of NACA 0012 aerofoil section, including the effects of upper-surface roughness simulating hoar frost. Technical memorandum 3726, Ministry of Defence: Aeronautical Research Council, January 1970.

[2] J. Johansen. Prediction of laminar/turbulent transition in airfoil flows. Technical memorandum, Riso National Laboratory, Roskilde, Denmark, May 1997.

[3] D. Rutherford and M. Zeinali. Efficiency trends for new commercial jet aircraft: 1960 to 2008, November 2009. [Online; accessed 27-May-2015]. URL: http://www.theicct.org/sites/default/files/publications/ICCT_Aircraft_Efficiency_final.pdf.

[4] World Bank. Air transport, passengers carried, 2014. [Online; accessed 27-May-2015]. URL: http://data.worldbank.org/indicator/IS.AIR.PSGR.

[5] IATA. A global approach to reducing aviation emissions, November 2009. [Online; accessed 27-May-2015]. URL: http://pp-www.iata.org/whatwedo/environment/Documents/global-approach-reducing-emissions.pdf.

[6] H. Schlichting. *Boundary-Layer theory.* McGraw-Hill, 2000.

[7] J. Stack. Compressible flows in aeronautics. *Journal of Aeronautical Science*, **12**(2):127–143, April 1945.

[8] B. Aupoix, D. Arnal, H. Bézard, B. C. F. Chedevergne, S. Deck, V. Gleize, P. Grenard, and E. Laroche. Transition and turbulence modeling. *Journal AerospaceLab*, **2**:1–13, March 2011.

[9] J. Mans. *Streak development and breakdown during bypass transition*. PhD thesis, Eindhoven University of Technology, March 2007.

[10] H. L. Reed and W. S. Saric. Stability of three-dimensional boundary layers. *Annual Review of Fluid Mechanics*, **21**:235–284, 1989.

[11] Boeing Commercial Airplane Corporation. Natural laminar flow airfoil analysis and trade studies: Final. Contract Report 159029, NASA, 1978.

[12] T.-J. Wu. Visualization of stall characteristics of airfoils using the smoke-wire techniques. Master's thesis, University of Texas at Arlington, December 1992.

[13] R. B. Langtry and F. R. Menter. Correlation-based transition modeling for unstructured parallelized computational fluid dynamics code. *AIAA Journal*, **47**(12):2894–2906, December 2009.

[14] I. H. Abbott and A. E. von Doenhoeff. *Theory of Wing Section.* Dover Publications Inc., 1959.

[15] D. M. Somers. Design and experimental results for a natural laminar flow airfoil for general aviation applications. Technical memorandum 1861, NASA, June 1981.

[16] H. J. Price. FAA Forecase Fact Sheet[1]-Fiscal Years 2011-2031, February 2011. [Online; accessed 10-June-2015]. URL: https://www.faa.gov/news/fact_sheets/news_story.cfm?newsId=12440.

[17] NASA. Environmentally responsible aviation project: Real solutions for environmental challenges facing aviation. AIAA, ASM, 2012.

[18] Skyline Magazine. ”Bringing Sustainable Air Transport Closer: Clean Skies - Special Edition”, June 2012. [Online; accessed 27-May-2015]. URL: http://www.cleansky.eu/sites/default/files/documents/cs-te-assessment-special-edition-2012.pdf.

[19] P. M. Peeters, J. Midel, and A. Hoolhorst. Fuel efficiency of commercial aircraft: An overview of historical and future trends. Technical Report 669, Netherlands National Aerospace Laboratory NLR, November 2005.

[20] J. E. Penner, D. H. Lister, D. J. Griggs, D. J. Dokken, and M. McFarland. Ipcc special report: Aviation and the global atmosphere. Technical report, Intergovernmental Panel on Climate Change, 1999.

[21] F. Collier. Fundamental aeronautics program subsonic fixed wing project reference document. [Online; accessed 17-November-2008]. URL: http://www.aeronautics.nasa.gov/nra_pdf/sfw_proposal_c1.pdf.

[22] Boeing Commercial Airplane Corporation . Press Release: “Boeing 787 Dreamliner Livery Change Enhances Airplane Performance , 2014. [Online; accessed 27-May-2015]. URL: http://www.boeing.com/commercial/news/2006/q3/060710d_nr.html.

[23] C. P. van Dam. Aircraft design and the importance of drag prediction and reduction. VKI Lecture Series 2003-2: CFD-Based Aircraft Drag Prediction and Reduction, National Inst. of Aerospace, November 2003.

[24] W. A. Basha and W. S. Ghaly. Drag prediction in transition flow over airfoils. *Journal of Aircraft*, **44**(3), 2007.

[25] V. N. Constantinescu. *Laminar Viscous Flow.* Mechanical Engineering Series. Springer, New York, New York, 1995.

[26] J. D. Anderson Jr. *Fundamentals of Aerodynamics.* McGraw Hill, fourth edition, 2005.

[27] A. L. Braslow. A history of suction-type laminar-flow control with emphasis on flight research. NASA History Division Office of Policy and Plans, 1999.

[28] J. E. Green. Laminar flow control-back to the future? page 3738, Seattle, Washington, June 2008. AIAA, 38th Fluid Dynamics Conference and Exhibit.

[29] D. M. Somers. Subsonic airfoil design: Historical background, 1999. [Online; accessed 10-June-2015]. URL: http://www.airfoils.com/design.pdf.

[30] M. S. Selig, M. D. Maughmer, and D. M. Somers. Natural-laminar-flow airfoil for general-aviation applications. *Journal of Aircraft*, **32**(4), 1995.

[31] R. B. Langtry. *A Correlation-Based Transition Model using Local Variables for Unstructured Parallelized CFD codes.* PhD thesis, University of Stuttgart, May 2006.

[32] T. Cebeci. *Stability and transition : theory and application : efficient numerical methods with computer programs.* Springer, Berlin, first edition, 2004.

[33] R. E. Mayle. The role of laminar-turbulent transition in gas turbine engines. *Journal of Turbomachinery*, **113**:509–537, 1991.

[34] W. S. Saric and H. L. Reed. Crossflow instabilities theory and technology. Reno, Nevada, January 2003. AIAA.

[35] K. Suder, J. O'Brien, and E. Reshotko. Experimental study of bypass transition in a boundary layer. Technical memorandum 100913, NASA, May 1988.

[36] M. V. Morkovin. On the many faces of transition. Dallas, Texas, 1969. Symposium on Viscous Drag Reduction, Plenum Press.

[37] M. Swoboda and W. Nitsche. Shock boundary-layer interaction on transonic airfoils for laminar and turbulent flow. *Journal of Aircraft*, **33**, 1996.

[38] O. Reynolds. An experimental investigation of the circumstances which determine whether the motion of water shall be direct or sinuous, and of the law of resistance in parallel channels. *Philosophical Transactions of the Royal Society*, **174**:935–982, 1883.

[39] B. J. Abu-Chunnam and R. Shaw. Natural transition of boundary layers - the effects of turbulence, pressure gradient, and flow history. *Journal of Mechanical Engineering Science*, **22**(5):213–228, 1980.

[40] E. V. Driest and C. Blumer. Boundary layer transition: Freestream turbulence and pressure gradient effects. *AIAA Journal*, **1**(6):1303–1306, 1962.

[41] D. D. Pasquale, A. Rona, and S. Garrett. A selective review of CFD transition models. 39th Fluid Dynamics Conference, San Antonio, Texas, June 2009. AIAA.

[42] X. Zheng, C. Lui, F. Liu, and C.-I. Yang. Turbulent transition simulation using the k-w model. *International Journal for Numerical Methods in Engineering*, **42**:907–926, 1988.

[43] H. Choi and P. Moin. Grid-point requirements for large eddy simulation: Chapman's estimates revisited. *Centre for Turbulence Research*, **1**, 2011. Annual

Briefs.

[44] P. R. Spalart. Strategies for turbulence modelling and simulations. *International Journal of Heat and Fluid Flow*, **21**:252–263, 2000.

[45] J. Smagorinsky. *Monthly Weather Review*, **91**(3):99–164, 1991.

[46] M. Germano, U. Piomelli, P. Moin, and W. H. Cabot. A dynamic subgrid-scale eddy viscosity model. *Physics of Fluids A*, **3**(7):1760–1765, 1991.

[47] V. Michelassi, J. G. Wissink, J. Frohlich, and W. Rodi. Large eddy simulation of a flow around a turbine blade with incoming wakes. *AIAA Journal*, **41**(1):2143–2156, November 2003.

[48] W. M. Orr. The stability or instability of the steady motions of a perfect liquid and of a viscous liquid. part i: A perfect liquid. In *Mathematical and Physical Sciences*. Proceedings of the Royal Irish Academy, 1907.

[49] A. Sommerfeld. Ein beitrag zur hydrodynamischen erklaerung der turbuenten fluessigkeitsbewegungen. In *Proceedings of the 4th International Congress of Mathematicians*, 1908.

[50] A. M. O. Smith and N. Gamberoni. Transition, pressure gradient and stability theory. Technical report, Douglas Aircraft Division, August 1956. ES 26388.

[51] J. L. van Ingen. A suggested semi-empirical method for the calculation of the boundary layer transition region. Technical report, Univ. of Deft, Dept. Aerospace Engineering, Delft, The Netherlands, 1956. Rep. VTH-74.

[52] Y. Suzen and P. Huang. Modeling of flow transition using an intermittency transport equation. Technical Report 209313, University of Kentucky, NASA, September 1999.

[53] F. Menter, T. Esch, and S. Kubacki. 5th transition modelling based on local variables. Mallorca, Spain, 2002.

[54] C. L. M. H. Navier. Memoire sur les lois du mouvement des fluides. *Mem. Acad. Roy. Sci.*, **6**:389–416, 1823.

[55] J. L. Stokes. On the theories of the internal friction of fluids in motion. *Transactions of the Cambridge Philosophical Society*, **8**:287–305, 1846.

[56] S. K. Nadarajah. *The discrete adjoint approach to aerodynamic shape optimization.* PhD thesis, Stanford University, 2003.

[57] P. Khayatzadeh. *Aerodynamic Shape Optimization of Natural Laminar Flow (NLF) Airfoils via Discrete Adjoint Approach.* PhD thesis, McGill University, December 2012.

[58] B. Walther. *Adjoint-based constrained aerodynamic shape optimization for multistage turbomachines.* PhD thesis, McGill University, 2014.

[59] A. Jameson and T. Baker. Solution of the euler equations for complex configurations. Danvers, MA, July 1983. AIAA, 6th Computational Fluid Dynamics Conference. 83-1929.

[60] J. Blazek. *Computational Fluid Dynamics: Principles and Applications.* Elsevier, first edition, 2001.

[61] D. C. Wilcox. *Turbulence Modeling for CFD.* DCW Industries, third edition, 2006.

[62] J. Boussinesq. Essai sur la théorie des eaux courantes. *Mémoires présentés par divers savants à l'Académie des Sciences*, **23**(1), 1877.

[63] R. W. Johnson. *The Handbook of Fluid Dynamics.* CRC Press, 1998.

[64] F. R. Menter. Improved two-equation k-w turbulence models for aerodynamics flows. Technical Report 103975, NASA, Ames Research Center, Moffet Field, California, October 1992.

[65] P. R. Spalart and C. L. Rumsey. Effective in flow conditions for turbulence models in aerodynamic calculations. *AIAA Journal*, **45**(10):2544–2553, October 2007.

[66] W. P. Launder and B. E. Launder. The calculation of low-Reynolds-number-phenomena with a two-equation model of turbulence. *International Journal of Heat and Mass Transfer*, **16**, 1973.

[67] D. C. Wilcox. Reassessment of the scale-determing equation for advances turbulence models. *AIAA Journal*, **26**, 1988.

[68] F. R. Menter. Zonal two equation k-omega turbulence models for aerodynamic flows. *AIAA Journal*, **32**(8):1598–1605, August 1994.

[69] F. Menter. Two-equation eddy-viscosity turbulence models for engineering applications. *AIAA Journal*, **32**(8):1598–1605, August 1994.

[70] F. R. Menter, R. B. Langtry, S. R. Likki, Y. B. Suzen, P. G. Huang, and S. Volker. A correlation-based transition model using local variables—part i: Model formulation. *Journal of Turbomachinery*, **128**, 2006.

[71] K. Chien. Predictions of channel and boundary-layer flows with a low-Reynolds-number turbulence model. *AIAA Journal*, **20**(1):33–38, 1982.

[72] P. Malan, K. Suluksna, and E. Juntasaro. Calibrating the $\gamma - re_\theta$ transition model for commercial CFD. In *47th Aerospace Sciences Meeting including, The New Horizons Forum and Aerospace Exposition*, Orlando, Florida, January

2009. AIAA.

[73] N. A. Denisse, D. A. Yoder, and N. J. Georgiadis. Implementation and validation of a laminar-to-turbulent transition model in the wind-us code. Technical memorandum NASA/TM2008-215451, Glenn Research Center, Cleveland, Ohio, September 2008.

[74] K. Suluksna, P. Dechaumphai, and E. Juntasaro. Correlations for modeling transitional boundary layers under influences of freestream turbulence and pressure gradient. *International Journal of Heat and Fluid Flow*, **30**(66-75):August, 2009.

[75] R. Ritlop, P. Khayatzadeh, and S. K. Nadarajah. Design of wind turbine profiles via a preconditioned adjoint-based aerodynamic shape optimization. In *47th Aerospace Sciences Meeting including, The New Horizons Forum and Aerospace Exposition*, Orlando, Florida, January 2009. AIAA.

[76] H. T. Kim, S. J. Kline, and W. C. Reynolds. The production of turbulence near a smooth wall in a turbulent boundary layer. *Journal of Fluids Mechanics*, **50**(1):133–160, December 1971.

[77] S. J. Kline, W. C. Reynolds, F. A. Schraub, and P. W. Runstadler. The structure of turbulent boundary layers. *Journal of Fluid Mechanics*, **30**(4):741–773, July 1967.

[78] P. R. Spalart. Direct simulation of a turbulent boundary layer up to Re=1410. Technical memorandum 89407, NASA, 1986.

[79] A. Jameson, W. Schmidt, and E. Turkel. Numerical solutions of the euler equations by finite volume methods with runge-kutta time-stepping schemes.

[80] J. Douglas, Jr. Alternating direction methods for three space variables. *Numerische Mathematik*, **4**(1):41–63, 1962.

[81] C. Hirsch. *Numerical Computation of Internal and External Flows: Volume 1 and 2.* John Wiley and Sons Inc., 1990.

[82] J. W. R. Taylor. *Jane's all the world's aircraft.* Jane's Information Group, 1978.

[83] Air Research Technology Inc. *Wing Extension and Spar Reinforcement Installation Guide 172: For Cessna 170, 172 and 175 models modified in accordance with Transport Canada STC SA01-35.*, second edition, 2011.

[84] R. Michel. Étude de la transition sur les profiles d'ailes; etablissement d'un critére de determination de point de transition et calcul de la trainee de profile incompressible. Technical report, Onera, 1951. Report 1/1578A.

[85] J. G. Schepers, A. Brand, A. Bruining, J. Graham, D. G. I. M.M Hand, H. A. M. HA, R. Paynter, and D. Simms. Final report of iea annex xiv: field rotor aerodynamics. Technical report, Netherlands Energy Research Foundation, 1997. ECN-C-97-027.

[86] R. R. Brodeur and C. P. van Dam. Transition prediction for a two-dimensional Reynolds-averaged Navier–Stokes method applied to wind turbine airfoils. *Wind Energy*, **4**:61–75, 2001.

[87] H. Sobieczky. DLR-F5: Test wing for CFD and applied applications. Technical report, DLR German Aerospace Research Establishment, 1994.

[88] H. Sobieczky. DLR-F5. [Online; accessed 23-June-2015]. URL: http://www.as.dlr.de/hs/DLR_F5/DLR-F5.htm.

[89] A. Mosahebi and E. Laurendeau. Convergence characteristics of fully and loosely coupled numerical approaches for transition models. *AIAA Journal*, **53**(5), 2015.

[90] C. Grabe and A. Krumbein. Corrleation-based transition transport modeling for three-dimensional aerodynamic configurations. *Journal of Aircraft*, **50**, 2013.

[91] J. G. Coder and M. D. Maughmer. Computation fluid dynamics compatible transition modeling using an amplification factor transport equation. *AIAA Journal*, **52**(11):2506–2512, 2014.